Remote Sensing of Environment 332 (2026) 115053

Contents lists available at ScienceDirect

Remote Sensing of Environment

journal homepage: www.elsevier.com/locate/rse

Three decades evolution of land subsidence driven by anthropogenic activities in the Yellow River Delta (YRD) from continuous SAR interferometry

Wenbin Xu [a], Jinheng Liu [a], Lei Xie [a,*], Mimi Peng [b], Hao Wang [c]

[a] School of Geosciences and Info-Physics, Central South University, Changsha 410083, China
[b] School of Information Mechanics and Sensing Engineering, Xidian University, Xi'an 710071, China
[c] The Second Institute of Hydrogeology and Engineering Geology, Shandong Provincial Bureau of Geology & Mineral Resources (Lubei Geo-engineering Exploration Institute), Dezhou 253000, China

ARTICLE INFO

Editor: Jing M. Chen

Keywords:
InSAR
Yellow River Delta
Land subsidence
Long-term monitoring
Time series linkage

ABSTRACT

The Yellow River Delta (YRD) has experienced severe subsidence due to anthropogenic activities. However, no study has resolved continuous deformation and investigate its mechanism across a three-decade timeframe from InSAR perspective since the early 1990s. This study proposes a Trend-Adaptive Functional Modeling and Connection method (TAFMC) for multi-sensor InSAR time series integration, with features of adaptability, robustness, and efficiency. It enables the identification of continuous deformation trends previously obscured by data gaps, thereby directly supporting the discovery of decadal deformation evolution. Second, six InSAR sensors were integrated to retrospect to the ground deformation in YRD from 1992 to 2024. The connected InSAR time series indicates three decades of subsidence, caused by deep groundwater extraction, reached up to 220 cm in Guangrao County. But the subsidence has been effectively controlled from >10 cm/yr during 1992–2021 to ~5 cm/yr after 2021. Since 2015, an inland migration of a coastal subsidence funnel occurred due to the brine industry. Multiple small-scale subsidence funnels with rates exceeding 15 cm/yr emerged, linked to shrimp aquaculture around 2023. These findings provide comprehensive insights for the interaction between anthropogenic activities and the YRD subsidence on a decadal scale, and offer a methodological framework applicable to InSAR multi-decadal analysis in other delta regions.

1. Introduction

Delta regions, sustaining over 350 million inhabitants and hosting numerous megacities, play a crucial role in global economy, industry, agriculture, and transportation (Anthony et al., 2024; Syvitski et al., 2009). However, more than 33 delta regions worldwide suffer significant land subsidence from 5 to 30 mm/yr (Syvitski et al., 2009), due to urbanization (Dong et al., 2014), reduced sediment (Edmonds et al., 2023), and resource extraction (Zhang et al., 2019a). In some deltas, such as the Yellow River Delta, China (Wang et al., 2022a), and the Mekong River Delta, Vietnam (Minderhoud et al., 2018), the rates of land subsidence even exceed global sea level rise by an order of magnitude. This exacerbates the vulnerability to land loss and coastal flooding (Shirzaei and Bürgmann, 2018), as well as the infrastructure deterioration such as cracks and fissures (Fig. S1). Therefore, accurate monitoring of deltaic subsidence and clarifying deformation mechanisms can effectively contribute to coastal risk mitigation (Fang et al., 2022).

Interferometric Synthetic Aperture Radar (InSAR), a high-resolution geodetic technique, has been widely used for monitoring land subsidence in deltas (Minderhoud et al., 2018; Wang et al., 2022a). In the YRD, one of China's largest delta regions, InSAR studies have revealed subsidence patterns in two feature areas, Dongying City and Guangrao County since the 1990s. For example, during 1992–2000, a subsidence funnel was discovered related to oil extraction in Dongying City, with a rate larger than 30 mm/yr (Zhang et al., 2015). From 2007 to 2010, the maximum subsidence rate of Dongying was 40 mm/yr, while Guangrao County suffered a significant subsidence with a rate exceeding 150 mm/yr due to groundwater extraction (Liu et al., 2016, Zhang et al., 2019a). Additionally, in the coastal aquaculture areas, a small subsidence funnel

* Corresponding author.
E-mail address: leixie_geo@csu.edu.cn (L. Xie).

https://doi.org/10.1016/j.rse.2025.115053
Received 4 June 2025; Received in revised form 5 September 2025; Accepted 27 September 2025
Available online 8 October 2025

with a subsidence rate exceeding 250 mm/yr was identified (Higgins et al., 2013). Since the 2010s, the subsidence rate in Guangrao remained at 150 mm/yr, while subsidence in Dongying City decreased both in extension and rate (Peng et al., 2020). However, a large subsidence funnel has appeared in the coastal region since 2015, in which the brine extraction contributed to over 94 % in the newly emerged coastal funnel (Wang et al., 2022a). More recently, the large coastal funnel in the YRD slowed down from 2020 to 2021, with this change potentially attributed to the impacts of the COVID-19 lockdown (Zhang et al., 2024b).

However, existing InSAR-based analyses in YRD focuses on short-term investigation with individual satellite (Wang et al., 2022a, Zhang et al., 2024b) or temporally fragmented due to observational gaps across multiple sensors (e.g., Fig. S2) (Liu et al., 2023; Zhang et al., 2021), constraining interpretation of anthropogenically driven subsidence/uplift processes on the decadal scale (e.g., hydrocarbon production and aquifer extraction).

Technically, given the typical 5–10 years operational lifespan of individual SAR satellite, multi-sensor temporal integration becomes essential for constructing seamless deformation time series. The temporal connection methods of InSAR time series can be classified as: 1) For connection with overlapped observation periods (e.g., Radarsat-2 and Sentinel-1), methods like quantile-quantile adjustment (QQA) (Li et al., 2023) and minimum gradient difference achieve high precision through temporal constraints (Chen et al., 2021). 2) More importantly, for temporally disconnected periods from earlier satellites (e.g., ERS and ENVISAT pre-2010s), functional modeling such as linear (Haghshenas Haghighi and Motagh, 2019), hyperbolic (Park and Hong, 2021), or logistic (Dong et al., 2023) functions typically serve as prior bridging constraints. These existing methods conduct time series linkage either global fitting using uniform functional model across all segments (Lu et al., 2025) or separated fitting followed by weighted cumulative deformation linkage during non-overlapping periods (Fu et al., 2025). However, the global fitting suffers when deformation characteristics deviate substantially from the assumed functional model; and the separated fitting lacks temporal constraints between the gap period that small errors could be propagated. In addition, the existing methods impose a uniform functional method across heterogeneous deformation patterns, lacking the clarification and evaluation for the suitability of function models for distinct deformation patterns. Specifically, to enable broad fitting within a unified framework, existing studies typically favor nonlinear models over adaptively selecting models tailored to individual trends. However, the high computational demands of such nonlinear approaches introduce practical limitations when applied to large-scale and long-duration time series scenarios, and they are not universally applicable to all deformation patterns.

To address the gaps both in decadal YRD deformation mechanism and InSAR time series connection, this study attempts to: 1) Develop a Trend-Adaptive Functional Modeling and Connection method (TAFMC) for multi-sensor InSAR time series integration. It adaptively fits to diverse deformation trends, and enable large-scale applications with

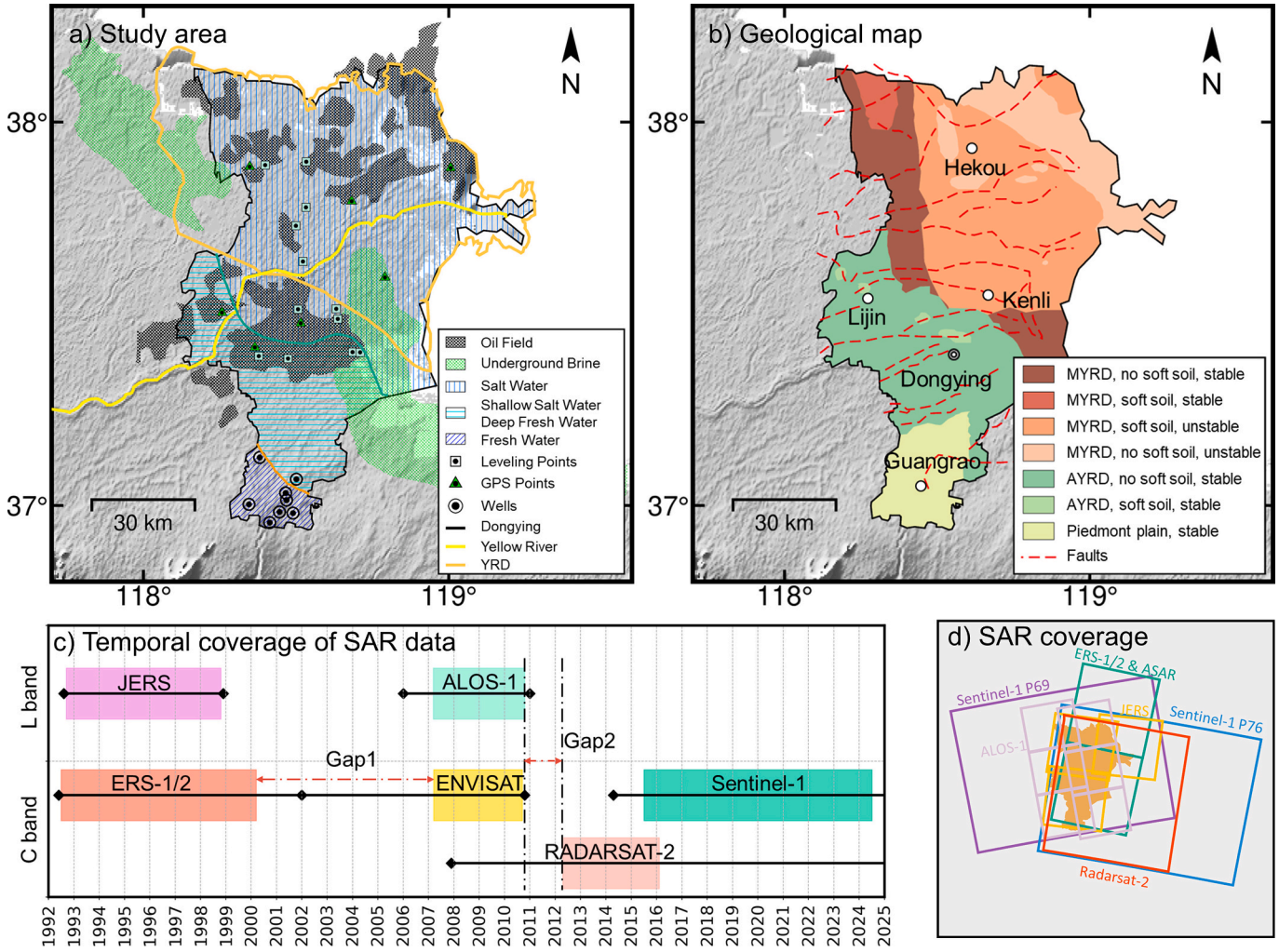

Fig. 1. Study area and datasets: a) The geography and aquifer information of the YRD. b) The geological map of the study area. c) Temporal coverages of SAR images. d)The footprints of SAR images used in this study. YRD boundary is refer to Wang et al. (2022a).

lower computational burden; 2) Comprehensively investigate three-decade YRD deformation since 1992, with most of available SAR datasets: ERS-1/2, JERS, Envisat ASAR, ALOS-1, Radarsat-2, and Sentinel-1. Thereby, for the first time, retrieving three decades of YRD deformation map in a spatial-temporal continuous frame, and providing comprehensive insights into the anthropogenic driving mechanisms.

2. Study area and data

2.1. Study area

The YRD is mainly located in Dongying City, Shandong Province, China, formed by the sediment carried by the Yellow River (Fig. 1a). The region has flat terrain, with an average elevation less than 6 m (Syvitski et al., 2009), and the terrain gradually decreases from southwest to northeast. The area is characterized by developed extensional fault structures, but no significant tectonic movement. Geologically, the YRD can be divided into the modern YRD (MYRD) and ancient YRD (AYRD) separating by the event of 1855 Yellow River diversion (Fig. 1b). The soils in the top 25 m are mainly composed of Holocene alluvial layers, such as fine sand, silt, and clay. MYRD is more compressible and more prone to consolidation than AYRD due to its shorter sedimentation history. Therefore, the MYRD has a lower compression modulus E_s (2.48–2.66 MPa) in the top 10 m of the sedimentary layer than the AYRD areas (2.50–3.20 MPa).

The YRD is rich in petroleum and brine resources. For the petroleum resource, YRD hosts the second largest oilfields, Shengli Oilfield, in China. Since the 1950s, over 1 billion tons of crude oil have been extracted (Liu et al., 2016). For the brine resource, the underground brine reserves in the shallow layer (<100 m) of the northeastern estuary, Dongying District, and Guangrao County (Fig. 1a) are estimated to total around 1 billion m^3, with an exploitable brine volume of approximately 600 million m^3 (Zhang et al., 2023).

However, the fresh groundwater is scarce, with most located in the southern part of Guangrao County (Liu et al., 2023) (Fig. 1a). The aquifers in the shallow, medium-depth, and deep groundwater layers are primarily composed of fine sand and fine silt, while low-permeability layers consist of clay, sandy clay, and silty clay (Liu and Huang, 2013). Agriculture, industry, and household water accounts for 52 %, 30 %, and 18 % of groundwater usage, respectively. Shallow groundwater primarily supports agriculture, while industrial consumption depends on deep groundwater. Subsidence funnels have developed in both shallow and deep groundwater layers.

2.2. Datasets

2.2.1. SAR satellite data

To comprehensively analyze the deformation evolution in YRD, we collected the data spanning the past three decades (1992–2024) from six SAR satellites (Fig. 1c-d). Table 1 lists the basic parameters of the SAR data used in this study. The dataset includes: 1) the stripmap (SM) data: 30 ERS-1/2 images, 50 JERS images, 122 ALOS-1 images, 56 Envisat ASAR images, and 2) Interferometric Wide-swath (IW) mode: 236 Sentinel-1 ascending images and 140 descending images. The Radarsat-2 data spanning 2012–2016 is from the existing research (Peng et al., 2020).

To ensure a complete coverage of the study area, we mosaicked the ERS-1/2 and Envisat ASAR frames 2835 and 2853, the ALOS-1 frames 730, 740, and 750 from path 445, the ALOS-1 frames 730, 740, and 750 of path 444, and 3 descending orbits of JERS data. Notably, there is a 7-year gap between ERS-1/2 and Envisat ASAR data (2000–2007), as well as a 2-year gap between Envisat ASAR and Radarsat-2 (2010−2012), and an overlap period between Radarsat-2 and Sentinel-1 data (2015–2016).

2.2.2. In-situ measurements

To validate the InSAR time series and explore the deformation mechanism, two types of in-situ geodetic measurements are used (Fig. 1a). The first is 11 sites of leveling measurement conducted between 2012 and 2016 using the Trimble DiNi03 digital level with instrumental accuracy of 0.3 mm. Loop misclosures were constrained within $\pm 4\sqrt{k}$ mm, where k denotes the length of the leveling route (in kilometers), and a least-squares adjustment was applied to process the leveling data. The second dataset consists of campaign GNSS measurements at six sites conducted between 2008 and 2010 using a Topcon-CR3 dual-frequency antenna. Measurements were conducted in April and October each year, with over 24 h of continuous observation, a sampling rate of 30 s, and an elevation angle of 10–20°. GNSS data were processed under ITRF2008 reference frame using the GAMIT/GLOBK software (Herring et al., 2010), with corrections for ionosphere and modeled troposphere. The estimated vertical deformation accuracy of the GNSS data is better than 10 mm. We also collected shallow groundwater levels measured by tape and ammeter from 1992 to 2023 at 8 locations.

3. Method

This section introduces the data processing steps and the proposed TAFMC method (Fig. 2). First, multi-source SAR data are processed

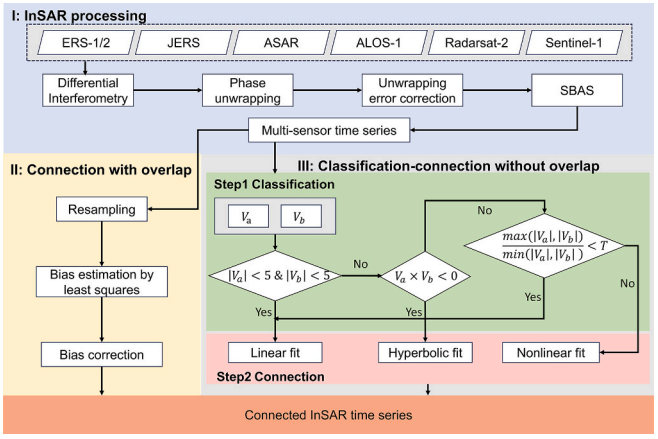

Fig. 2. Flowchart of the proposed method: I) InSAR processing; II) Connection of InSAR time series with temporal overlaps; III) Connection of InSAR time series for non-overlapping InSAR time series.

Table 1
Parameters of the SAR Datasets.

SAR Sensor	Period	Total acquisitions	Incidence angle	Orbit direction	Resolution (Az × Rg)/m
Sentinel-1	20150701–20240526	236	39	Ascending	20 × 5
	20161005–20211214	140	39	Descending	
Radarsat-2	20120430–20160620	12	26	Descending	30 × 26
Envisat ASAR	20070201–20100903	56	23	Descending	4 × 8
ALOS-1	20070129–20101109	122	39	Ascending	3 × 8
ERS-1/2	19920511–20000413	30	23	Descending	4 × 8
JERS	19920827–19980905	50	39	Descending	5 × 9

using time-series InSAR technique to obtain deformation time series for each sensor (Fig. 2 I). Then, the InSAR deformation time series from each sensor are connected in two scenarios. Specifically, for time series with overlapping periods, the bias during the overlap is calculated and used to correct the InSAR time series (Fig. 2 II). For InSAR time series without overlapping periods, a classification-connection strategy is applied (Fig. 2 III).

3.1. InSAR time-series processing

We used the GAMMA software to perform differential interferometric processing (Werner et al., 2000), with SRTM DEM applied to remove topographic contributions. For ERS-1/2, Envisat ASAR, ALOS-1, and Sentinel-1 data, single-look complex (SLC) images were used directly. For JERS data, the raw data are focused to SLC before the interferometry. For Sentinel-1, the Enhanced Spectral Diversity method was utilized to perform the fine co-registration and maintain the co-registration error less than 1/1000 pixel. We used the Minimum Cost Flow method to unwrap the interferograms. The triangular phase closure method was applied to detect unwrapping errors. We excluded interferograms with severe unwrapping errors that were spatially scattered and difficult to manually correct, and then manually corrected the remaining interferograms with unwrapping errors (See Text S1, Table S2, Fig. S4 in Supplementary Material for details).

The Small-Baseline Subset InSAR (SBAS InSAR) method was employed for the time series analysis (Berardino et al., 2002), with SAR interferogram pairs selected based on temporal and spatial thresholds (See Table S1 and Fig. S3). We only kept the pixels with spatial and temporal coherence >0.4. The atmospheric delays were mitigated by GACOS products (Yu et al., 2018). We removed the remaining orbital trend using a first-order or second-order plane. Finally, we corrected DEM errors based on the linear relationship with the perpendicular baselines before the time series estimation.

For the period with both ascending and descending Sentinel-1 observations (2016–2021), the LOS displacements were decomposed into vertical and east-west components by assuming negligible north-south deformation (Fialko et al., 2001):

$$\begin{bmatrix} d_{asc} \\ d_{desc} \end{bmatrix} = \begin{bmatrix} \cos(\theta_{asc}) & -\sin(\theta_{asc}) \bullet \cos(\varphi_{asc}) \\ \cos(\theta_{desc}) & -\sin(\theta_{desc}) \bullet \cos(\varphi_{desc}) \end{bmatrix} \bullet \begin{bmatrix} d_U \\ d_{EW} \end{bmatrix} \quad (1)$$

Here, θ_{asc} and θ_{desc} represent the incidence angles of the ascending and descending tracks, respectively; φ_{asc} and φ_{desc} denote the azimuth angles of the ascending and descending tracks; d_{asc} and d_{desc} are the LOS deformation time series for the ascending and descending tracks; and d_U and d_{EW} represent the vertical and east-west deformation components, respectively.

For periods with only single-track observations, the subsidence is projected by the incidence angle, as follows:

$$d_v(t) = \frac{d_{LOS}(t)}{\cos\theta} \quad (2)$$

in which $d_v(t)$ and $d_{LOS}(t)$ are time series of vertical and LOS deformations at time epoch t, respectively. θ denotes the incidence angles from SAR geometry. Except for the 2D deformation analysis over the oilfield area (Fig. 16), all deformation analyses in this study are based on vertical components (Dong et al., 2023).

3.2. The linkage of multiple InSAR time series

Here, we propose a TAFMC method for multi-sensor InSAR time series integration. This method provides a unified framework that considers different temporal coverages of sensors and different deformation patterns. The linkage process is first divided based on the temporal overlap of InSAR datasets, and then the non-overlapping deformation series are classified according to their distinct deformation trends. Tailored fitting functions are subsequently applied to each category to achieve adaptive connection of different deformation trends, balancing connection accuracy and computational efficiency.

3.2.1. The linkage of overlapped InSAR time series

To connect two time series with overlapping intervals, we directly calculated the bias during the overlapping period and used it to correct the subsequent series. For instance, the connection of Sentinel-1 and Radarsat-2 time series in this study, we linearly interpolated the Sentinel-1 time series during the overlapping period to match the timestamps of Radarsat-2. Biases between the two sensors were calculated for each time, and their temporal variations (caused by satellite geometry, atmospheric errors, and et al.) were averaged over the overlapping period. This average bias was applied to correct the Sentinel-1 time series. The bias calculation between the connection of InSAR time series with common temporal overlap can also be performed using more advanced computational methods, such as the Quantile-Quantile Adjustment (QQA) method (Li et al., 2023), which estimates the constant offset between two time series by comparing the probability distributions during their overlapping period.

3.2.2. The linkage of non-overlapping InSAR time series

For connecting InSAR time series without temporal overlaps, the key objective involves calculating the cumulative deformation during SAR temporal gaps (Fu et al., 2025). In this process, the advantage of the TAFMC method is particularly evident. We categorize all deformation time series based on their temporal evolution trends (the linear deformation rates of the time series to be connected) into four types: stable deformation time series, transition deformation time series between subsidence and uplift, linear deformation time series, and time series with highly nonlinear behavior (Table 2). For each category, we apply appropriate estimation strategies to maintain deformation trends while balancing computational efficiency (Fig. 3).

Let $\left\{\left(t_i^a, d_i^a\right)\right\}_{i=1}^m$ and $\left\{\left(t_j^b, d_j^b\right)\right\}_{j=1}^n$ denote two temporally non-overlapping deformation time series, where t denotes the observation time, and d denotes the deformation. The superscripts a and b indicate the preceding and succeeding periods, respectively. m and n represent the indices of SAR acquisition time. Accordingly, the two series for non-overlapping case should satisfy the condition in temporal domain, as $t_1^b > t_m^a$. Prior to connection, both series are typically normalized as $d_1^a = d_1^b = 0$. Then, the linear deformation velocity of v_a and v_b categorized the preceding and succeeding InSAR time series into the following four cases:

CASE I stable deformation time series: For stable time series with $|v_a| < 5$ and $|v_b| < 5$, a linear assumption is directly applied to estimate the cumulative deformation. Specifically, the average deformation rate for the missing period is determined by a time-weighted average from the preceding and following segments (Fig. 3a). Therefore, the cumulative deformation d_{gap} for the gap periods is:

Table 2
Deformation patterns and functional models used for TAFMC method.

Deformation type	Classification features	Functional models
Stable trend	$\lvert V_a\rvert, \lvert V_b\rvert < 5$ mm/yr	$y = at + b$
Parabola trend	$V_a \times V_b < 0$	$\begin{cases} d_i^a = at_i^{a\,2} + bt_i^a + c \\ d_j^b = at_j^{b\,2} + bt_j^b + c + d_{off} \end{cases}$
Linear trend	$\frac{max(\lvert V_a\rvert, \lvert V_b\rvert)}{min(\lvert V_a\rvert, \lvert V_b\rvert)} < T$	$y = at + b$
Exponential trend	$\frac{max(\lvert V_a\rvert, \lvert V_b\rvert)}{min(\lvert V_a\rvert, \lvert V_b\rvert)} > T$	$\begin{cases} d_i^a = ae^{bt_i^a} + c, t_i^a \\ d_j^b = ae^{bt_j^b} + c + d_{off} \end{cases}$

The detailed logical structure is illustrated in Fig. 2-III.

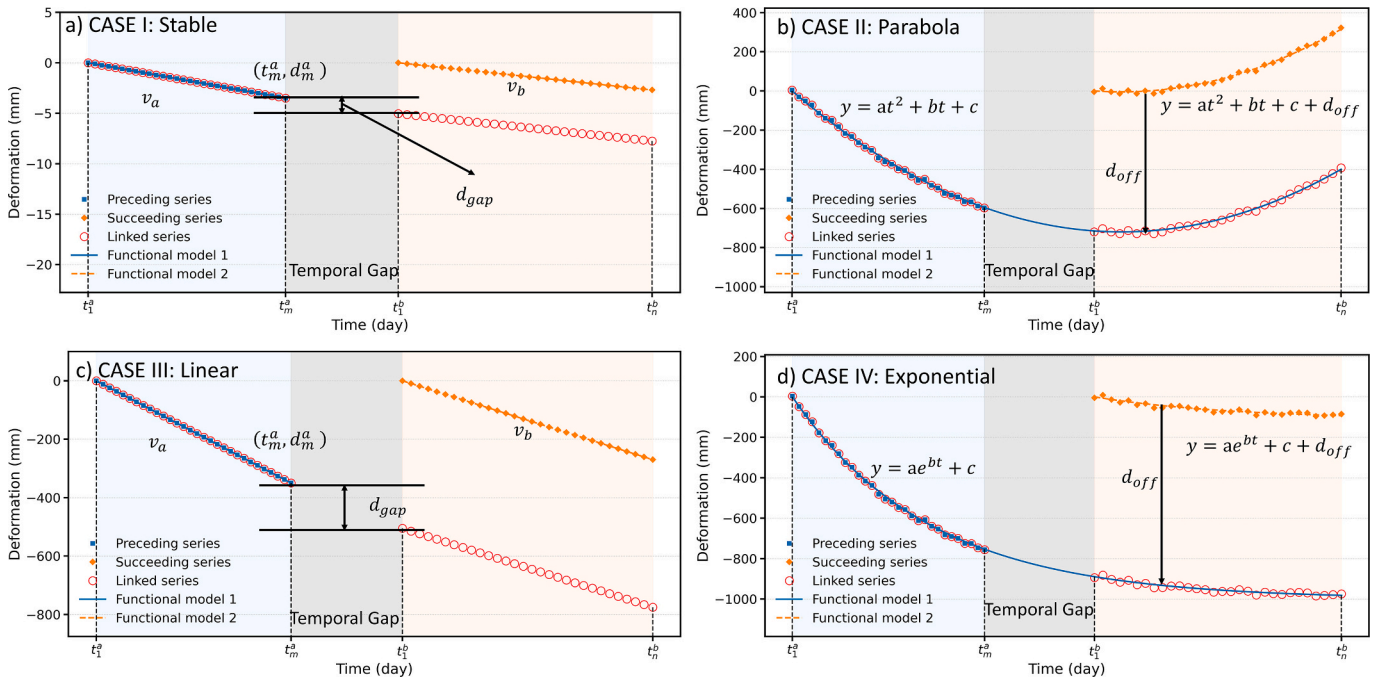

Fig. 3. Illustration of the TAFMC method for linking InSAR deformation time series exhibiting various trends without temporal overlap. a) CASE I: stable deformation time series. b) CASE II: Transition deformation time series between subsidence and uplift. c) CASE III: Linear deformation time series. d) CASE IV: Time series with highly nonlinear behavior. Please note the subplots have different ranges of y-axis for the purpose of illustration.

$$d_{gap} = \frac{v_a\left(t_m^a - t_1^a\right) + v_b\left(t_n^b - t_1^b\right)}{t_m^a - t_1^a + t_n^b - t_1^b} \times \left(t_1^b - t_m^a\right) \tag{3}$$

The adjusted time series is $d = \left\{d_i^a\right\}_{i=1}^{m} \cup \left\{d_j^b + d_m^a + d_{gap}\right\}_{j=1}^{n}$.

CASE II transition deformation time series between subsidence and uplift: For deformation pattern switches between subsidence and uplift, i.e., $v_a \times v_b < 0$, the deformation tendency is subject to a parabolic function. We fit the pre- and post- time series segments separately using a parabolic function to estimate the overall offset d_{off} (Eq. 4 and Fig. 3b), as follows:

$$\begin{cases} d_i^a = at_i^{a2} + bt_i^a + c, t_i^a \in \left[t_1^a, \ldots, t_m^a\right] \\ d_j^b = at_j^{b2} + bt_j^b + c + d_{off}, t_j^b \in \left[t_1^b, \ldots, t_n^b\right] \end{cases} \tag{4}$$

The adjusted time series is $d = \left\{d_i^a\right\}_{i=1}^{m} \cup \left\{d_j^b + d_{off}\right\}_{j=1}^{n}$.

CASE III linear deformation time series: For time series with a significant linear tendency, we compute the cumulative deformation during the gap period under the linear assumption, using the same approach as in CASE I. This case is identified as $\frac{\max(|V_a|,|V_b|)}{\min(|V_a|,|V_b|)} < T$, in which the threshold T for deformation magnitude is set to 3. This threshold T was determined through simulated time series with varying degrees of nonlinearity. The accuracy of time series linkage under both linear and nonlinear assumptions was compared, allowing the optimal threshold to be identified (please refer to Supplementary Text S2 and Table S3 for the detail of threshold determination).

CASE IV time series with highly nonlinear behavior: For time series with significant non-linear deformation, we identify this case as $\frac{\max(|V_a|,|V_b|)}{\min(|V_a|,|V_b|)} > T$. An exponential function (Fu et al., 2025) is used to estimate the overall offset d_{off} of the later segment (Fig. 3d), formulated as:

$$\begin{cases} d_i^a = ae^{bt_i^a} + c, t_i^a \in \left[t_1^a, \ldots, t_m^a\right] \\ d_j^b = ae^{bt_i^b} + c + d_{off}, t_j^b \in \left[t_1^b, \ldots, t_n^b\right] \end{cases} \tag{5}$$

The adjusted time series is $d = \left\{d_i^a\right\}_{i=1}^{m} \cup \left\{d_j^b + d_{off}\right\}_{j=1}^{n}$.

4. Results and analysis

4.1. Results of InSAR deformation

4.1.1. Accuracy validation

We assessed the accuracy of InSAR measurements for both internal and external accuracy. First, after projecting the obtained deformation onto the vertical direction, the correlation for Sentinel-1 ascending and descending tracks is 0.90 (Fig. 4a), and the correlation between the deformation rates of ALOS-1 and Envisat ASAR is 0.49 (Fig. 4b). The mean error for these two cross-sensor validations are 1.43 mm/yr and −1.05 mm/yr, respectively. These validations show the reliability of InSAR observation across different sensors. Second, we compared the InSAR results with external leveling and GNSS observations (Fig. 1a, sites marked as rectangles and triangles). During the 2008–2010, the GNSS matches well with the InSAR observation, with an RMSE of 0.4 cm/yr (Fig. 4c). From 2012 to 2016, the InSAR results show a similar tendency with the leveling data with an RMSE of 2.2 cm/yr (Fig. 4d). The specific numerical comparison between InSAR and in-situ measurement data can be found in Tables S4 and S5. In general, the InSAR results exhibit high accuracy in both inter and external validations.

4.1.2. Decades deformation in YRD from InSAR

Over the past three decades, the multiple InSAR observations show deformation in the YRD has been primarily concentrated in the oilfield area of Dongying urban region, the southern part of Guangrao County, and the coastal saltpan area (Fig. 5).

The subsidence in the Dongying oilfield region has reached to a maximum of 35 cm cumulative subsidence during 1992–2024 (Fig. 6). It also exhibits a high spatial correlation with the distribution of oilfields (Fig. 7), suggesting that oil extraction is the primary cause of surface subsidence (Liu et al., 2016). From 1992 to 1998, subsidence in this region was mainly concentrated in the Dongxin Oilfield and Shengtuo Oil Plant, with a maximum subsidence rate exceeding 30 mm/yr (Fig. 7a). During 2007–2010, subsidence in the Shengtuo Oil Plant area disappeared, while the Dongxin Oilfield area continued to experience subsidence, with a subsidence rate remaining around 30 mm/yr.

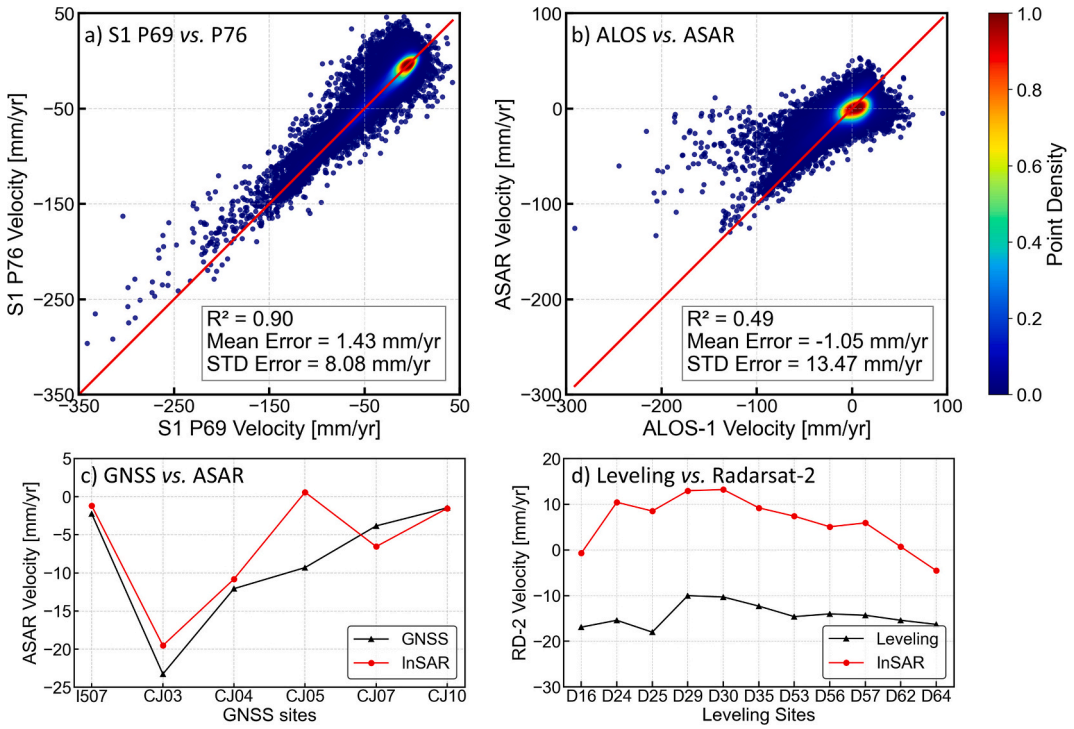

Fig. 4. Accuracy assessment of InSAR deformations. a) Comparison between Sentinel-1 ascending and descending tracks (2016–2021); b) Comparison between Envisat ASAR and ALOS-1 (2007–2010); c) Comparison between InSAR Envisat ASAR and GNSS (2008–2010); d) Comparison between Radarsat-2 and leveling measurements (2012–2016). See Fig. 1a for the location of GNSS and leveling sites.

Additionally, a new subsidence funnel covering more than 4 km^2 emerged in the Shinan Oilfield area (Fig. 7b). Between 2012 and 2016, the subsidence funnel in the Shinan Oilfield area persisted but slowed to approximately 20 mm/yr. The subsidence funnel in the Dongxin Oilfield area also disappeared (Fig. 7c). By the Sentinel-1 period (2015–2024), the subsidence funnels in the Dongying oilfield region had largely disappeared, with no significant deformation rate > 10 mm/yr (Fig. 7d).

The second prominent subsidence is in the southern region of Guangrao County (Fig. 8), which is caused by groundwater extraction (Liu et al., 2023). During the observational period of 1992–2024, the cumulative deformation in Guangrao is intensive with maximum subsidence of 220 cm, and approximately 80 km^2 of the area has experienced cumulative subsidence greater than 100 cm (Fig. 6). Between 1992 and 2000, ERS-1/2 images did not capture any significant subsidence in Guangrao County, while JERS images revealed a subsidence funnel covering approximately 100 km^2 with a subsidence rate exceeding 50 mm/yr. Given the dense temporal coverage and L-band data to better keep the coherence, we consider the JERS results is more reliable to reflect the deformation in Guangrao before 2000s. During 2007–2010, the subsidence rate exceeded 150 mm/yr, forming two subsidence funnels in Lean and Dawang (Fig. 8b), with the most severe subsidence of 170 mm/yr. Between 2012 and 2016, the extent and rate of the subsidence funnels is similar to 2007–2010. From 2015 to 2024, the subsidence funnels expanded, and the center of the subsidence funnel shifted from Dawang to the Lean.

Third, in the coastal saltpan area, high-intensity subsidence emerged around 2015 (Fig. 9), with a maximum annual subsidence rate exceeding 400 mm/yr. The primary driving factor for subsidence is related to the underground brine extraction (Wang et al., 2022a). During the periods from 1992 to 1998 and from 2007 to 2010, no significant deformation was observed in the coastal saltpan area. In addition, unlike the two aforementioned subsidence areas, the coastal saltpan region exhibited no measurable deformation signal during the Radarsat-2 phase (2012–2016). This is mainly due to changes caused by the construction and operation of the saltpan, which reduced coherence, combined with the limited number of Radarsat-2 acquisitions. In general, the maximum cumulative deformation in the coastal saltpan area exceeds 170 cm, as recorded during the Sentinel-1 observation period.

4.2. *Continuous temporal evolution*

For InSAR time series with overlapping period, the connection steps described in Section 3.2.1 was used to connect the Sentinel-1 and Radarsat-2 time series (Fig. 10). The connected time series effectively preserves the deformation trend. In some areas, subsidence ceased aftr a period of time and even uplift occurred.

For InSAR time series without overlapping period, the connection steps described in Section 3.2.2 was used to connect the Radarsat-2 and Envisat ASAR time series (Fig. 11). For time series with sustained stability, extensive processing is unnecessary, and a linear assumption does not introduce significant errors. Although the limited temporal resolution and lower signal-to-noise ratio of Radarsat-2 constrain the reliability of the connection, the InSAR deformation trend can still be well preserved.

By analyzing the subsidence time series and annual subsidence rates from 2015 to 2024 (Fig. 12), surface uplift phenomenon was identified in the severely subsiding northeastern coastal saltpan area and the southern part of Guangrao County.

We selected characteristic points in the uplifted area to analyze the process of transitioning from subsidence to uplift. The time series in the coastal subsidence area exhibits little seasonal variation, with a generally stable subsidence rate (Fig. 13c). Surface uplift of approximately 2 cm occurred from August 2019 to the end of 2019, and around 5 cm from April 2021 to April 2022. These deformation patterns strongly suggest human intervention. In the southern subsidence area of Guangrao County, subsidence remained largely linear from 2007 to 2021, with minor fluctuations in the subsidence rate. From July 2021 to January 2023, a surface uplift of 5 cm was observed, displaying a clear cyclical pattern (Fig. 13e).

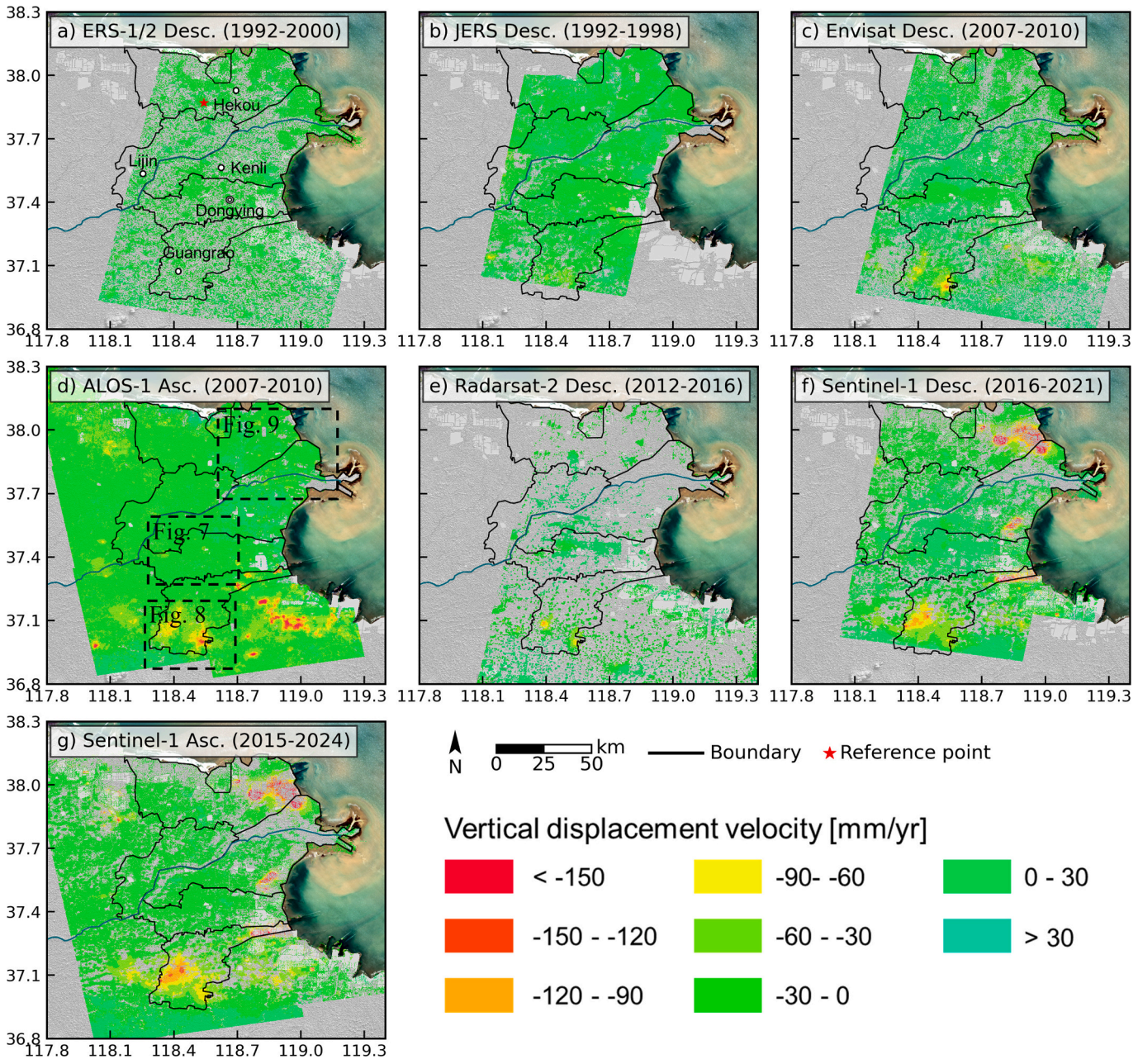

Fig. 5. Vertical deformation rate from multiple InSAR data (negative values indicate subsidence). a) ERS-1/2 descending, b) JERS descending, c) Envisat ASAR descending, d) ALOS-1 ascending, e) Radarsat-2 descending, f) Sentinel-1 descending and g) Sentinel-1 ascending. The extents of Figs. 7–9 are marked as dash boxes in panel d).

5. Discussion

5.1. Diversified surface deformation of oilfields in YRD

Oil extraction reduces reservoir pressure, leading to reservoir compression and subsequent surface subsidence. To enhance oil production, injection of water, CO_2, or other substances are often adopted to increase reservoir pressure and facilitate oil flow, which may cause surface uplift (Hu et al., 2020; Qu et al., 2023; Wang et al., 2022b). Long-term monitoring of deformation in oilfield areas enables a better understanding of the deformation evolution caused by oil extraction process. Here, we analyzed 2 sites of oilfields to show the varying deformation evolution in YRD during the recent three decades (Fig. 14).

The Dongxin oilfield is one of the earliest oilfields in northern China. It was officially put into operation in 1968 and transitioned to water injection development in 1971. From 1991 to 1995, the average annual oil production was 2.75 million tons, followed by a gradual decline in production (Liang, 2011). This coincides with InSAR time series as a period of relatively high subsidence rates from 1992 to 1998, gradually slowing between 2007 and 2010. After 2012, as oil wells were shut down, subsidence gradually ceased.

The Shinan Oilfield, a fault-block oilfield developed in the late 1970s, did not exhibit significant surface subsidence from 1992 to 1998. However, it showed relatively uniform subsidence from 2007 to 2016, which gradually stopped after 2016. This may reflect the formation pressure was not exhausted during oil extraction in 1992–1998. In contrast, during 2007–2016, the water injection rate was insufficient to maintain the reservoir pressure under continuous oil extraction (Qu et al., 2023). Subsequently, the field reached injection-production balance or ceased operation, leading to surface stabilization.

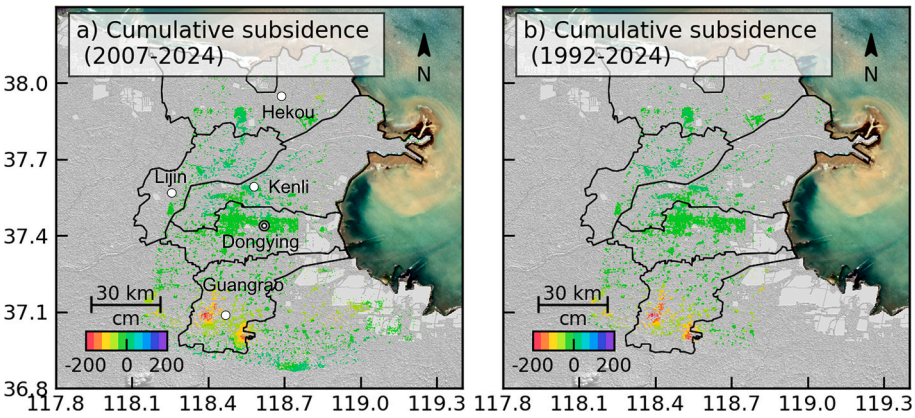

Fig. 6. Cumulative subsidence of YRD: a) 2007–2024 and b) 1992–2024. Note that the deformation map in 1992–2024 is more sparse and incomplete in the south of Guangrao due to the 9-year gap between JERS and ASAR, and the incomplete coverage of JERS.

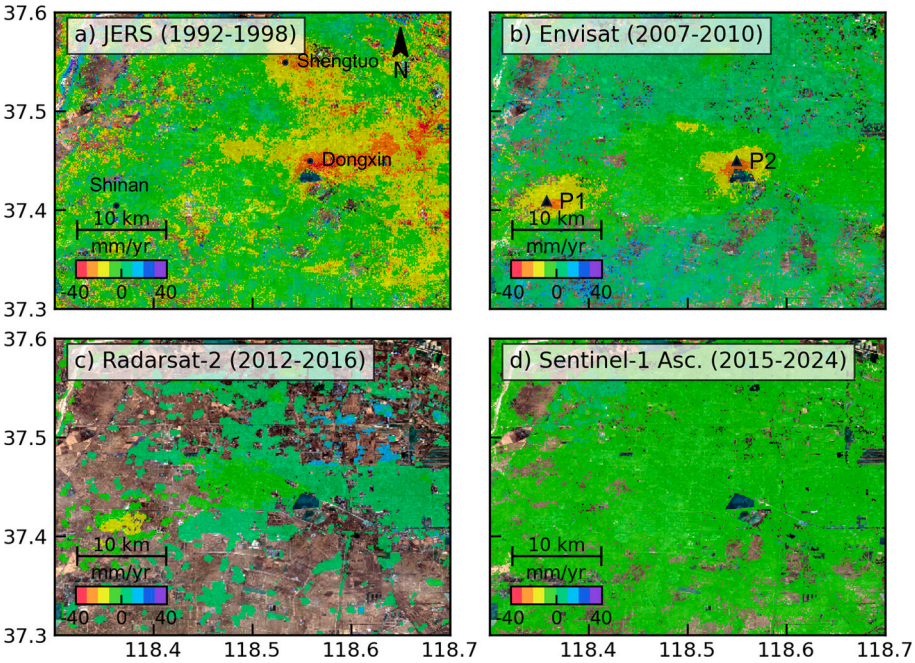

Fig. 7. Vertical deformation rate of oilfields in Dongying: a) 1992–1998, b) 2007–2010, c) 2012–2016, d) 2015–2024.

In oilfield regions of the YRD, we observed two featured surface deformation patterns. For P5 point (Fig. 15a, c), the surface initially experienced uplift at a rate of 10 mm/yr from 2008 to 2010, followed by approximately six years of subsidence during 2012–2018. This is attributed to fluid injection driving oil toward production wells, followed by subsidence during subsequent oil extraction. While formation pressure dissipation could also explain the subsidence (Qu et al., 2023), its magnitude, four times greater than the uplift, suggests it primarily resulted from oil extraction.

In another site P6 (Fig. 15b, d), the oilfield area experienced subsidence at a rate of 10 mm/yr during 2008–2010, followed by uplift at the similar rate during 2012–2016. This reflects the alternation of oil extraction (i.e., subsidence) and water injection (i.e., uplift), with initial oil extraction followed by subsequent water injection operations (Cun et al., 2024). However, detailed investigation for the deformation mechanism in oilfield should be supported by in-situ production data and numerical models.

In the southern oilfield region of Kenli District, horizontal deformation of up to 10 mm/yr was detected during the Sentinel-1 observation period (2016 to 2021) (Fig. 16). The horizontal and vertical components together form a cone-shaped deformation pattern. Notably, this horizontal deformation, significantly exceeding vertical deformation, is more likely associated to the water injection rather than the oil extraction, in which the vertical deformation is prominent (Tang et al., 2024). As the purpose of fluid injection is to push oil toward production wells (Esene et al., 2019), the horizontal movement of the fluid is more likely to induce horizontal deformation. As the fluid injection increases pore pressure on the fault plane, which may explain 12 earthquakes with maximum M 3.6 event reported in Kenli County during 1992–2024. A more comprehensive understanding of the deformation caused by water injection and its impacts necessitates further analysis incorporating detailed oilfield production data.

5.2. *The migration and emergence of coastal subsidence funnels in YRD*

In the recent decade (2015–2024), the InSAR results indicate coastal areas of YRD have the new migration of subsidence funnel, and emergence of new small-scale funnels. First, since 2015, a large subsidence funnel has developed in the eastern coastal area of Hekou County, with an area of over 500 km^2 where the subsidence rate exceeds 50 mm/yr,

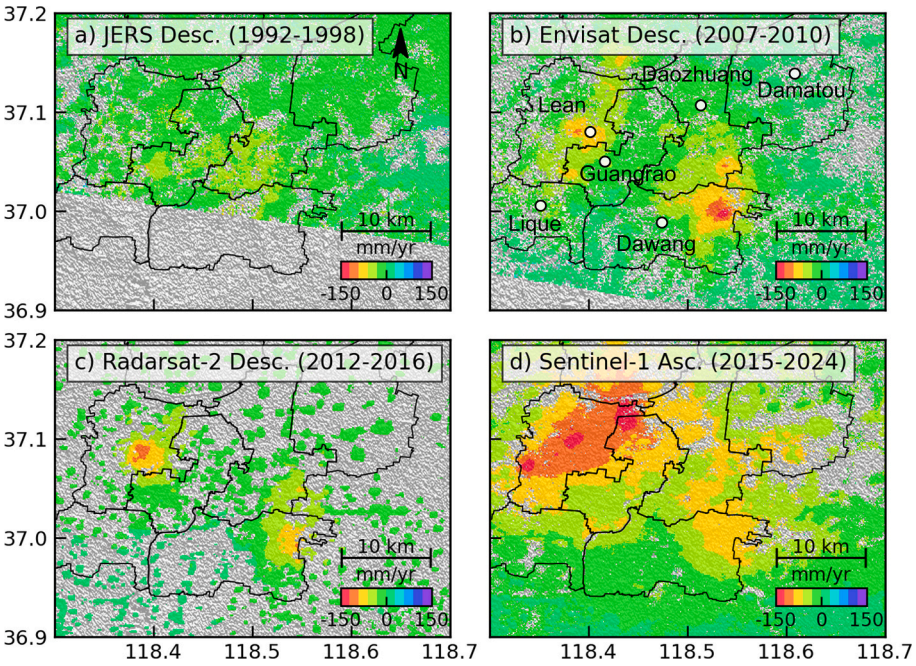

Fig. 8. Vertical deformation rate around Guangrao County: a) 1992–1998, b) 2007–2010, c) 2012–2016, and d) 2015–2024.

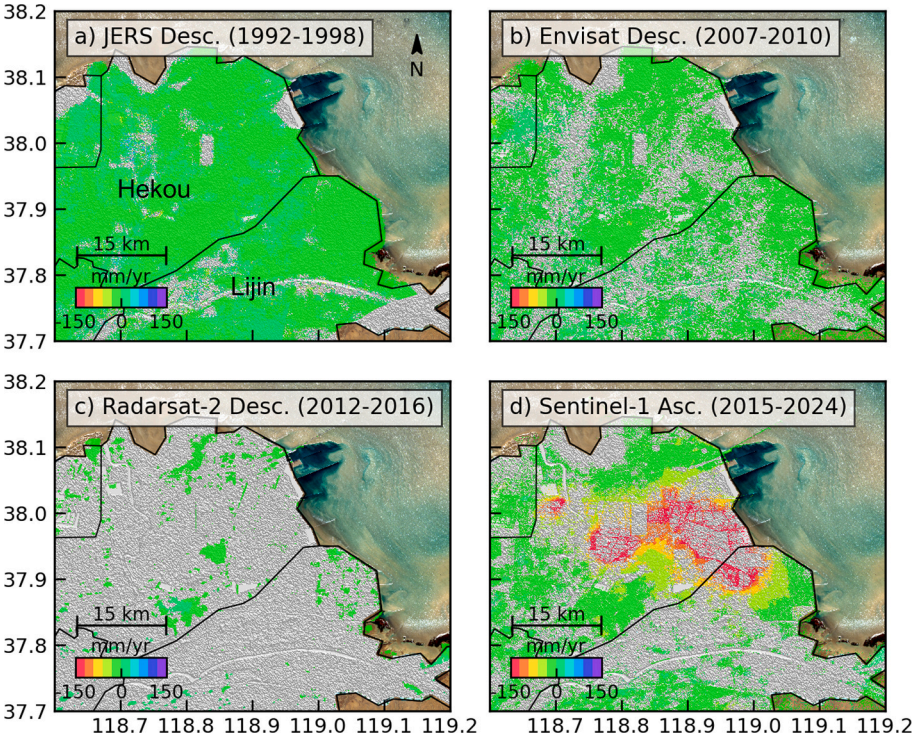

Fig. 9. Vertical deformation rates in the eastern part of Hekou County: a) 1992–1998, b) 2007–2010, c) 2012–2016, and d) 2015–2024.

and a maximum annual subsidence rate exceeding 400 mm/yr (Fig. 17a). The area with a subsidence rate greater than 50 mm/yr in the newly emerged subsidence funnel expanded from approximately 220 km^2 in 2015 to approximately 500 km^2 in 2020 (Fig. 17a-d). Subsequently, from 2020 to 2024, the subsidence center progressively shifted westward toward inland (Fig. 17f-h), and the extension of subsidence is narrow down.

To analyze the migration process, we applied the K-means clustering method to the subsidence time series (Festa et al., 2023). The time series were normalized to minimize the influence of subsidence magnitude, and the elbow method identified three optimal clusters (Fig. 18). The clustering result shows the Class 1 has a rapid subsidence from 2015 to July 2021 in an area of 180 km^2. It stabilized with no further subsidence from 2021 to 2024, and even experienced a brief surface uplift. In Class 2, subsidence progresses slowly from July 2015 to July 2018, then accelerates and maintains a stable subsidence rate from July 2018 to May 2024. In Class 3, a relatively high subsidence rate is observed between July 2015 and January 2021, followed by a deceleration in subsidence.

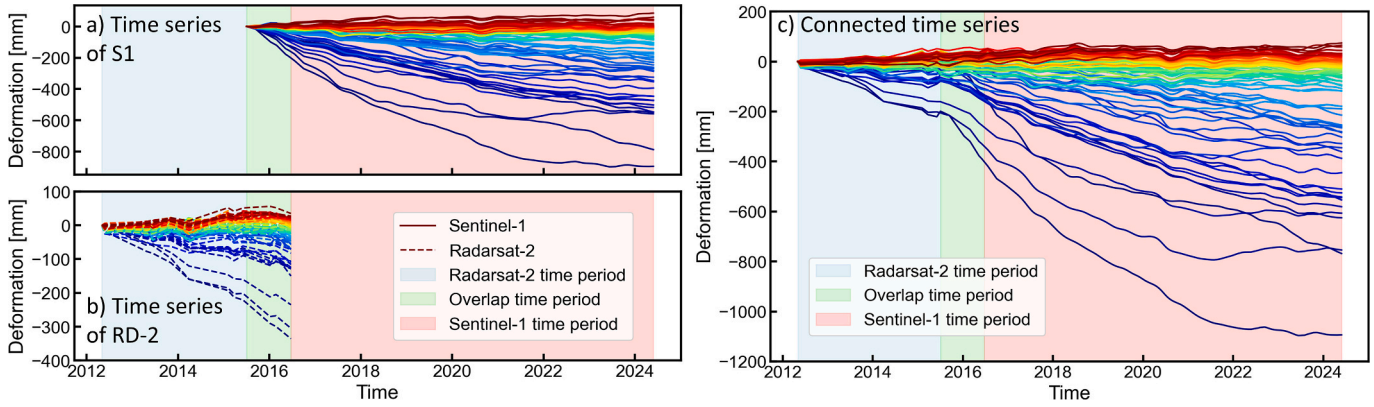

Fig. 10. Connection of Sentinel-1 and Radarsat-2 Time Series. a) Deformation time series derived from Sentinel-1 observations. b) Deformation time series derived from Radarsat-2 observations. c) Integrated time series obtained using the proposed method.

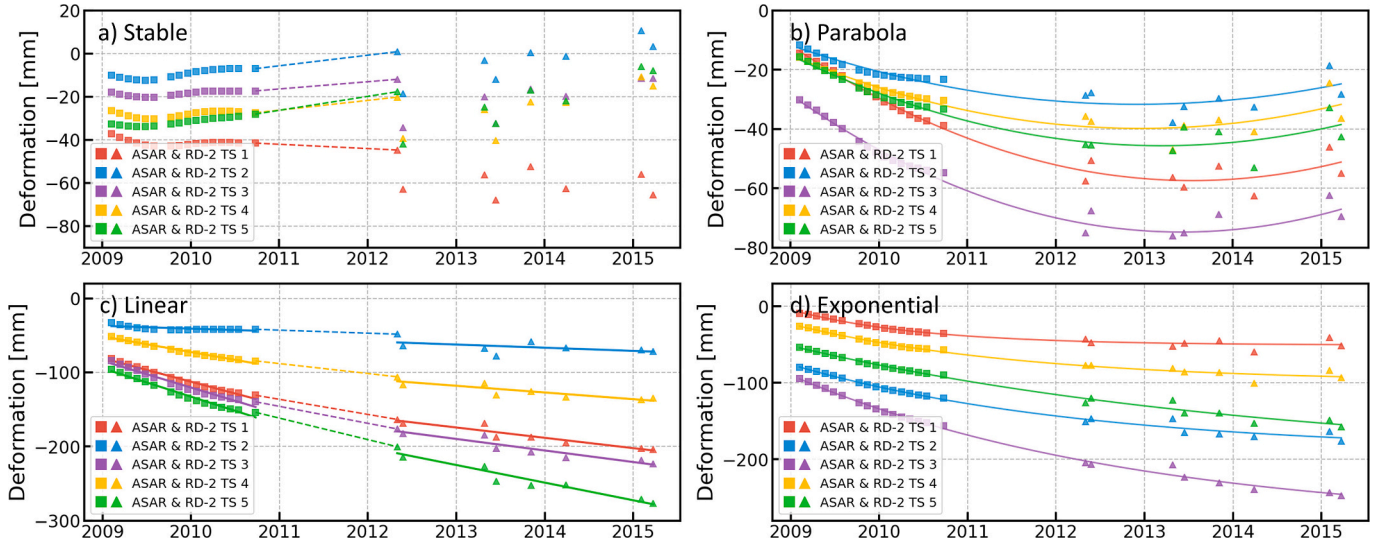

Fig. 11. Linkage of Envisat ASAR and Radarsat-2 InSAR time series. a) Stable deformation time series, b) Transitional time series between subsidence and uplift, c) Linear deformation time series, d) Time series with highly nonlinear behavior.

The approximately 180 km^2 subsidence funnel of Class 1 gradually disappeared after 2021. The subsidence center migrated southwestward inland by mid-2021.

The primary cause of the subsidence in Hekou County appears to be underground brine extraction for salt production and shrimp farming. Unlike water-soluble salt mining (Xing et al., 2024), this process direct pumping brine water. In this case, along with the presence of more than 15-m compressible soil layers in the area with compression modulus of 2.48–3.20 MPa, if groundwater does not replenish timely, severe subsidence will occur as observed in Hekou County. However, with brine concentrations decline, the economic viability reduced and eventually halting extraction, which explains the observed slowdown of subsidence and the mitigation since 2021.

The land use change also indicates an expansion of water bodies by 140 km^2 in coastal Region A since 2005 (118.75°–118.90° E, 37.90°–38.05° N; Fig. 19a-e). However, no significant surface subsidence was detected between 2005 and 2015. Two possible reasons may explain this observation: 1) Pre-2015 brine extraction remained limited, causing a mild decline of brine table, and the onset of surface subsidence lagged behind the extraction process (Tang et al., 2022). The snapshots of Sentinel-2 and Landsat-7/8 optical imagery confirm that the key indicators of active salt production, such as evaporation ponds and salt crust, has a very limited distribution (Fig. 19f-j). 2) Minor subsidence potentially occurred between 2010 and 2015 but the limited availability of Radarsat-2 imagery cannot provide reliable measurement in the changing coastal area.

In the subsidence center region during 2023–2024 (118.75°–118.90° E, 37.90°–38.05° N; Region B, Fig. 19), land subsidence demonstrates strong spatial correlation with water distribution patterns. In the first phase of 2012–2015, salt field construction commenced (Fig. 19k–i), and by 2015, a large number of salt production facilities had been established, accompanied by small-scale subsidence (Fig. 17a). Second, after 2015, no further expansion of salt field infrastructure was observed in Region B (Fig. 19i–o). Instead, intensive underground brine extraction began, leading to significant subsidence in Region B, reaching up to 150 mm/yr, and continued through 2024. The subsidence center progressively migrated inland from coastal zones toward Region B. Prolonged extraction in Region A likely should brine concentrations and increased operational costs, prompting activity transfer to Region B. Concurrently, surface uplift emerged in part of Region A (Fig. 13a) due to brine table recharge by seawater intrusion and precipitation infiltration.

Besides the large subsidence funnel in Hekou County, multiple small and scattered subsidence funnels have extensively emerged since January 2023 (Fig. 20). Zones Z1 to Z4 mark the approximate locations of these funnels, and their specific locations and areas of these small-scale subsidence funnels are listed in Table S6. These subsidence funnels have subsidence rates exceeding 100 mm/yr and are distributed across Hekou, Lijin, and Kenli counties, with the areas of the funnels

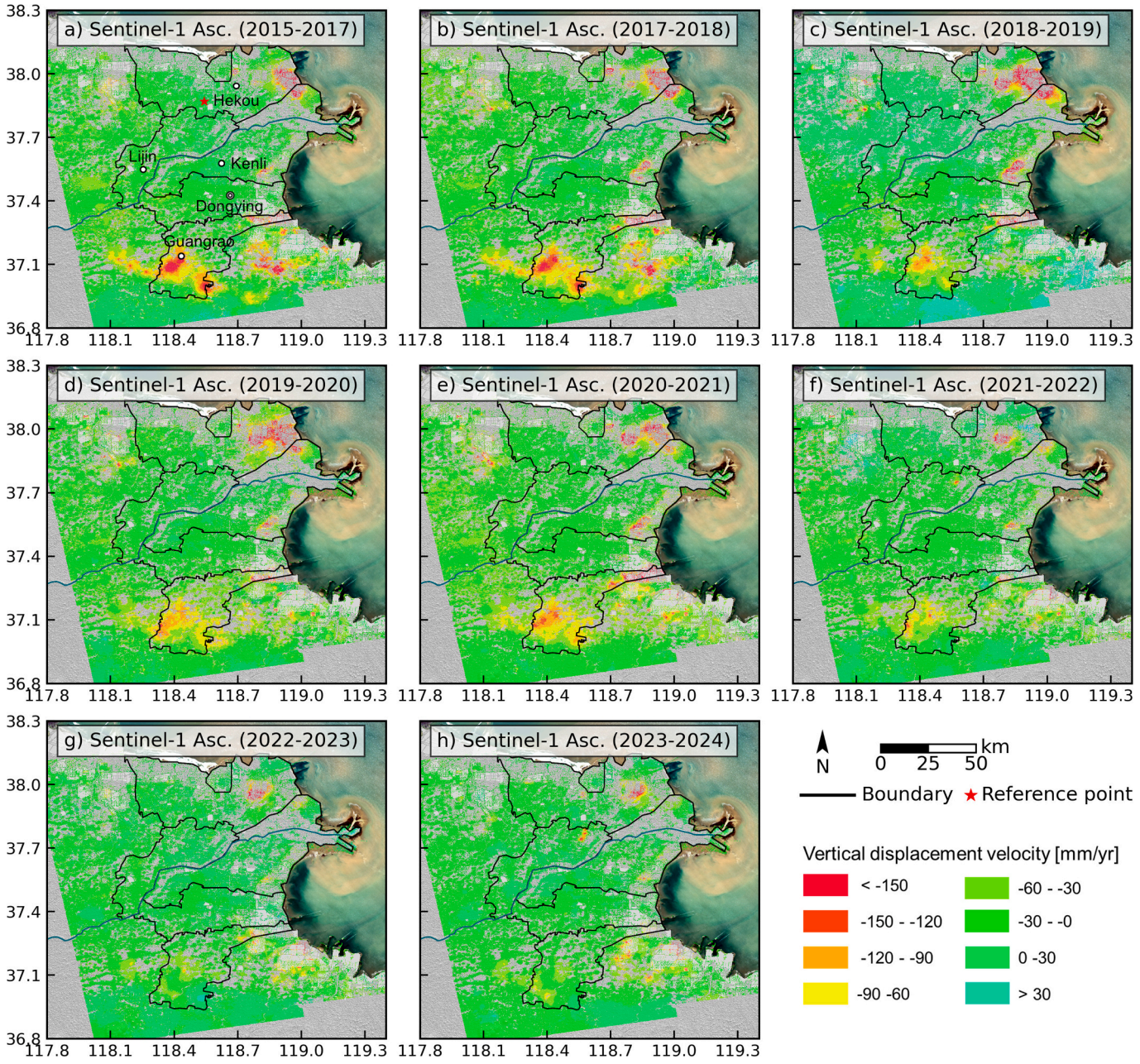

Fig. 12. Annual deformation rates in the YRD from 2015 to 2024.

ranging from a few square kilometers to several tens of square kilometers. These subsidence funnels are strongly associated with small-shed shrimp farming areas, and mainly located at MYRD with soft soil sediments, in which the higher porosity and lower compression modulus can cause significant compression, due to deceases of pore pressure and increases effective stress after brine extraction. Unlike coastal aquaculture, which extracts groundwater in the winter season (Higgins et al., 2013), small-shed shrimp farming relies entirely on brackish groundwater, thereby significantly increasing the demand for groundwater (Wang et al., 2022a). With the proliferation of small-shed shrimp farming, this high-intensity, small-scale surface subsidence may become one of the main types of subsidence in the Yellow River Delta region.

5.3. The response between surface deformation and groundwater in Guangrao County

Guangrao County hosts numerous chemical plants which exploit groundwater for industrial production, which is widely considered the primary cause of severe surface subsidence and a key factor shaping the region's spatiotemporal deformation patterns (Liu et al., 2023; Zhang et al., 2019a). However, the specific impact of shallow and middle-deep groundwater on subsidence has not been thoroughly discussed. Overall, the correlation between shallow groundwater level fluctuations and InSAR deformation time series in Guangrao County is low (as shown in Fig. 21), and shallow groundwater level fluctuations have minimal impact on subsidence rates. Moreover, shallow groundwater in Guangrao is primarily used for agricultural irrigation, which shows strong seasonal characteristics (Chen, 2022). However, at subsidence-prone sites (such as DY, DX, LZ, and DG), the InSAR deformation time series does not exhibit seasonal variations related to agricultural irrigation (as shown in Fig. 21). At sites with slower subsidence (such as DL, DXI, DN, and LS), although the InSAR time series shows stronger seasonal characteristics, the groundwater levels at these sites are on an upward trend with no decelerated subsidence from InSAR observations. Considering

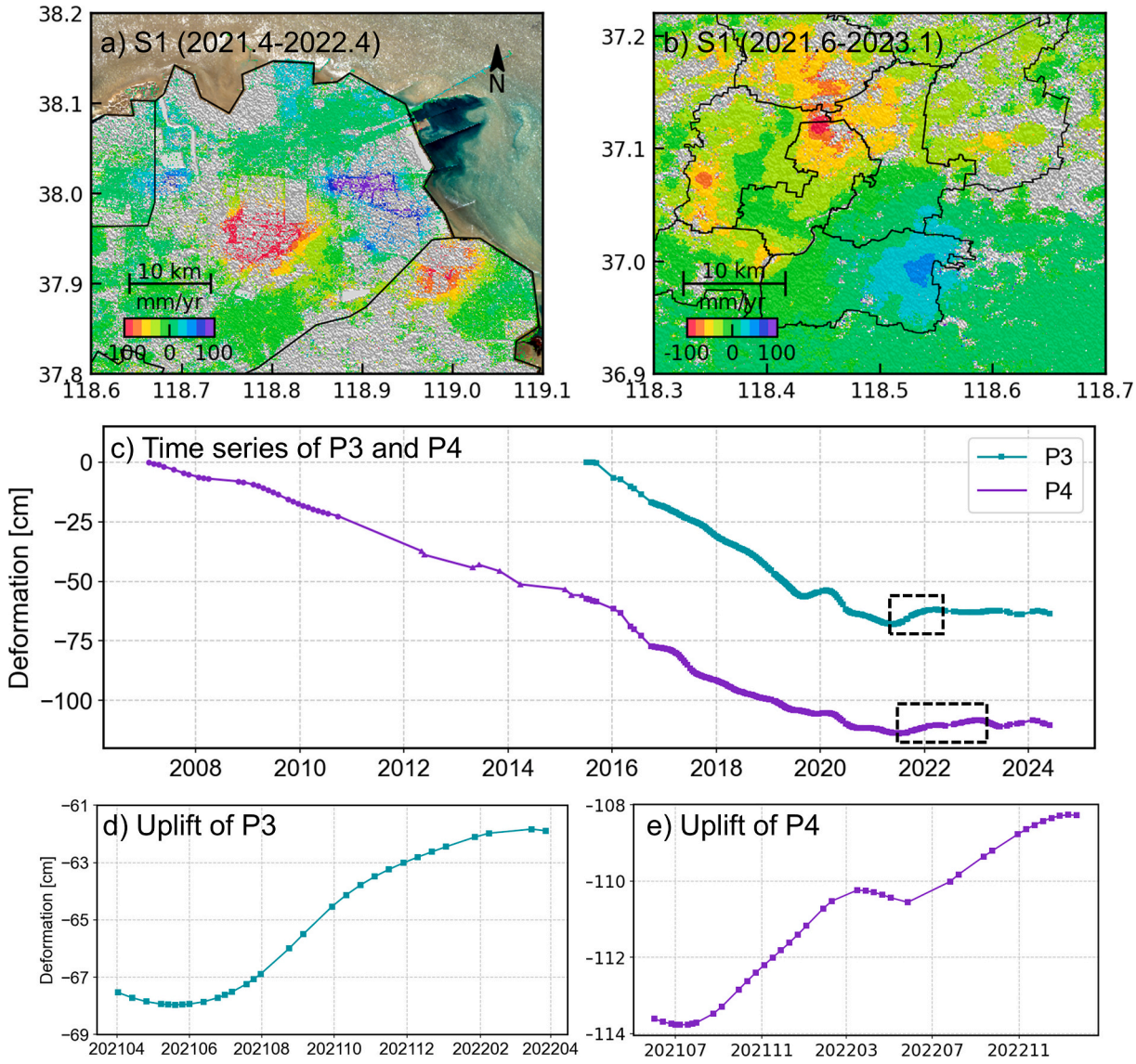

Fig. 13. Surface uplift observed in coastal salt fields (a, d) and southern Guangrao County (b, e).

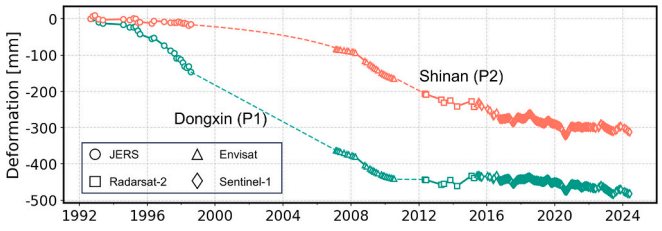

Fig. 14. Time series deformation in Shinan and Dongxin oilfields from 1992 to 2024. The site locations are depicted at Fig. 7b, noted as P1 and P2.

that the lithology of shallow groundwater aquifers in the region is mainly fine sand and medium-fine sand, with some medium-coarse sand and gravelly coarse sand, shallow groundwater level changes typically cause immediate elastic deformation (Zhao et al., 2024), without significant time delays. Therefore, we conclude that shallow groundwater level fluctuations are not the main factor influencing surface subsidence in this region.

Unlike shallow groundwater level changes, the total water consumption in Guangrao County shows a higher correlation with InSAR deformation (Fig. 21), particularly between 2021 and 2023. From 2021 to 2023, the total water consumption in Guangrao County decreased from 72 million m^3 to 53 million m^3, accounting for a decrease of approximately 26 %. Correspondingly, the InSAR subsidence rate was slowed down, even with parts of surface rebounds (Fig. 13b, e). The deceleration or uplift of land subsidence may be attributed to the reduction in middle and deep groundwater extraction, which allowed for the replenishment of deep groundwater aquifers. Although a reduction in shallow groundwater extraction could also contribute to the deceleration, at the sites where subsidence slowed significantly (DY, DX, LZ, DG), shallow groundwater levels had already risen before the significant reduction in water usage in 2021, without leading to a decrease in subsidence rate. This indicates that shallow groundwater is not effective in vertically replenishing middle and deep groundwater. The recovery of middle and deep groundwater mainly relies on lateral runoff replenishment (Shirzaei et al., 2019), in which different permeabilities of the rock and soil layers may change the groundwater dynamics, and drive the heterogeneously distributed spatial-temporal deformation (Duan et al., 2022).

5.4. Evaluation of the TAFMC method

In this section, we first compare the proposed TAFMC method with

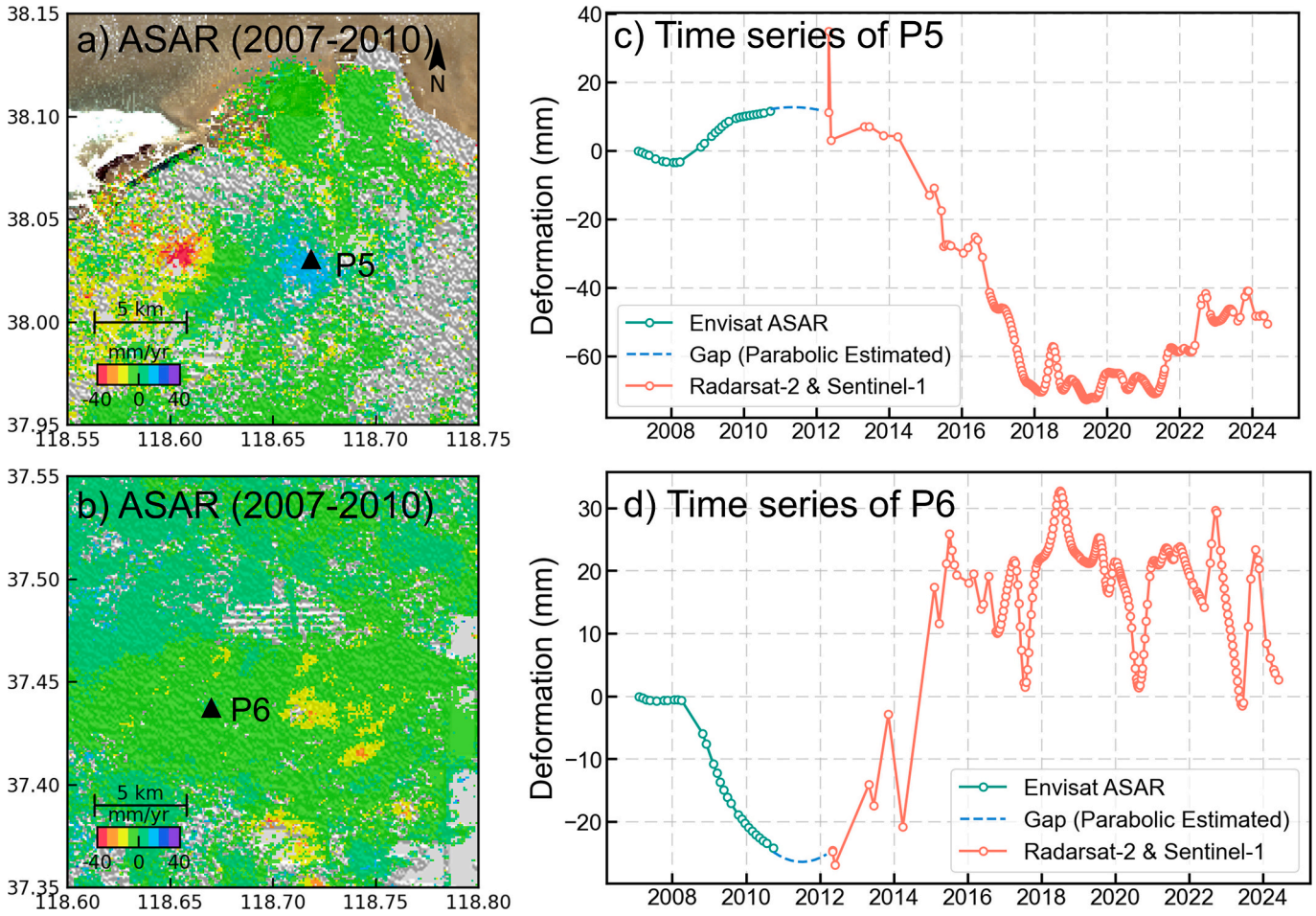

Fig. 15. Time series deformation of oilfields in the coastal area of YRD. a) and b) show the surface deformation rates of the oilfield areas obtained from Envisat ASAR data from 2007 to 2010. c) is the deformation time series from 2007 to 2024 at P5. d) is the deformation time series from 2007 to 2024 at P6.

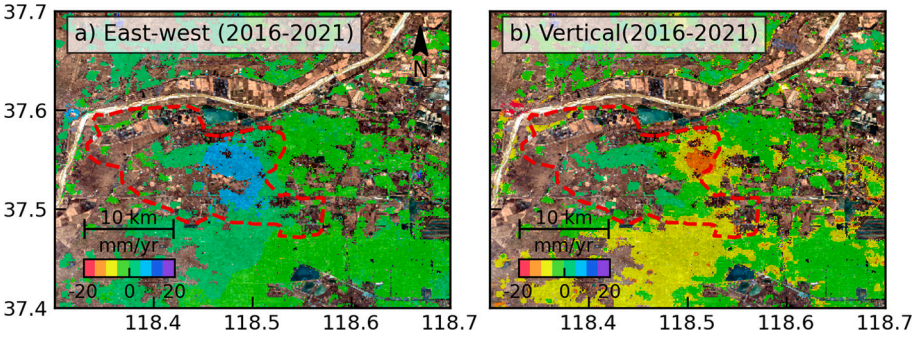

Fig. 16. Two-dimensional velocity from 2016 to 2021 in the Kenli Oilfield area from Sentinel-1: a) East-west velocity; b) Vertical velocity.

the conventional strategy that applies the single functional model to all deformation patterns. Second, the TAFMC method is benchmarked against nonlinear fitting techniques and Piecewise Exponential Fitting with Weighted Average (PEFWA; Fu et al., 2025).

To validate the necessity of classification prior to the time series linkage in the TAFMC method, we simulated the deformation time series using Bézier curves (Fu et al., 2025): Case 2–2000 entries, Case 3–4567 entries, and Case 4–5116 entries. In each entry, 87 samples have been simulated in 2000-day ranges with ±5 mm random noise, and a 400-days temporal gap has been setup. Linear fitting with two segments and nonlinear fitting were comparatively assessed (Table 3). For Case 2, we quantify the accuracy using the absolute fitting errors, as the cumulative deformation within the gap segment may approach zero in subsidence-to-uplift transitional patterns, making relative fitting errors potentially biased. The results indicate the two-segment linear model exhibited 47 % and 36 % increased fitting errors for parabolic and exponential deformation patterns, respectively. However, for the linear deformation as Case III, non-linear fitting has a 12 % accuracy decrease with substantial elevated computational cost. Therefore, the simulated experiments demonstrate that neither non-linear nor linear fitting can universally adapt to all deformation patterns. A classification should be conducted prior to the time series linkage to optimize accuracy and computational efficiency.

Second, we compared the TAFMC method with the PEFWA fusion

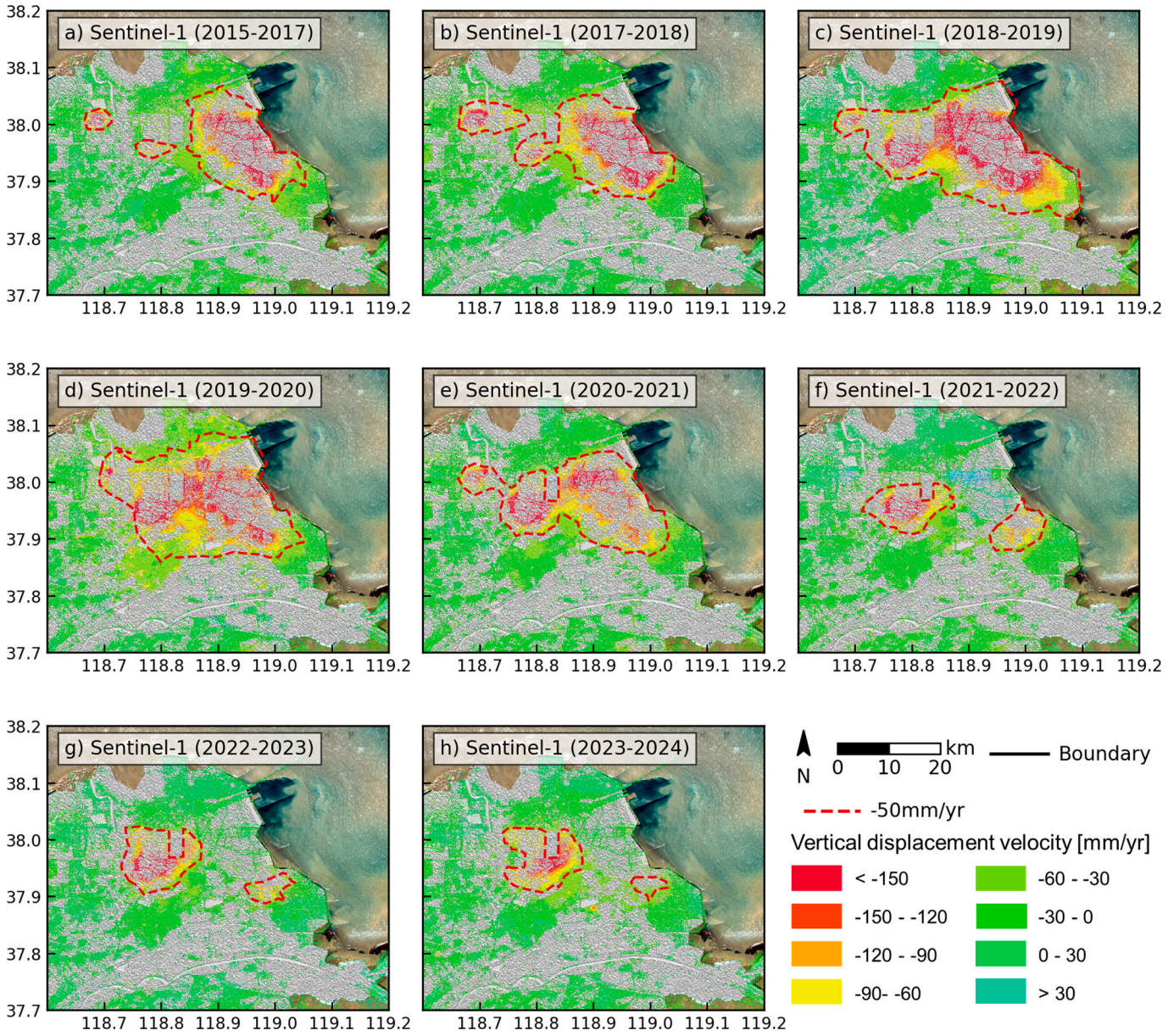

Fig. 17. Annual subsidence rates in the Yellow River Delta derived from Sentinel-1. The red dashed line represents the boundary of 50 mm/yr subsidence. (For interpretation of the references to colour in this figure legend, the reader is referred to the web version of this article.)

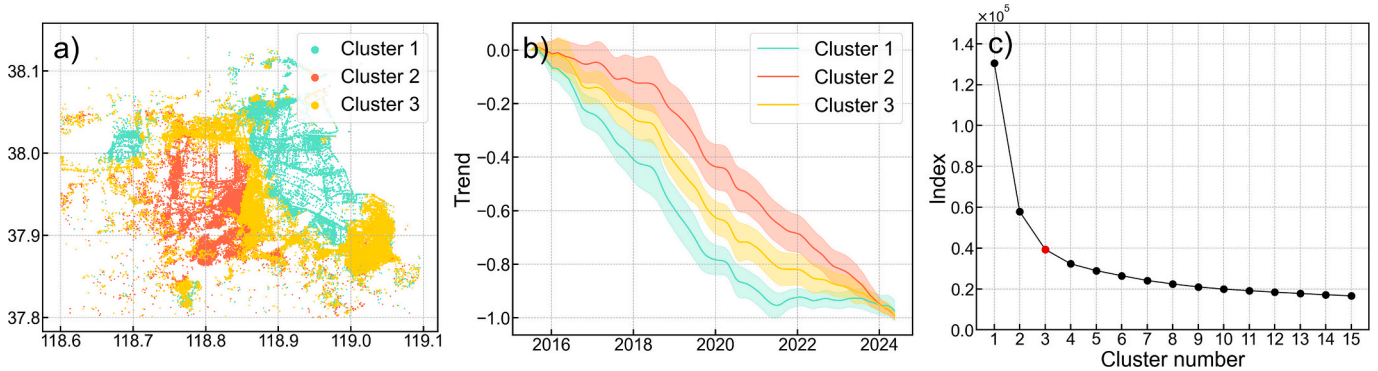

Fig. 18. K-means clusters for the subsidence funnel in the eastern part of Hekou County. The average subsidence rates for Clusters 1, 2, and 3 are 67 mm/yr, 57 mm/yr, and 49 mm/yr, respectively. a) Spatial distribution of clusters. b) Temporal evolution of different deformation patterns. c) Elbow method to determine the number of clusters.

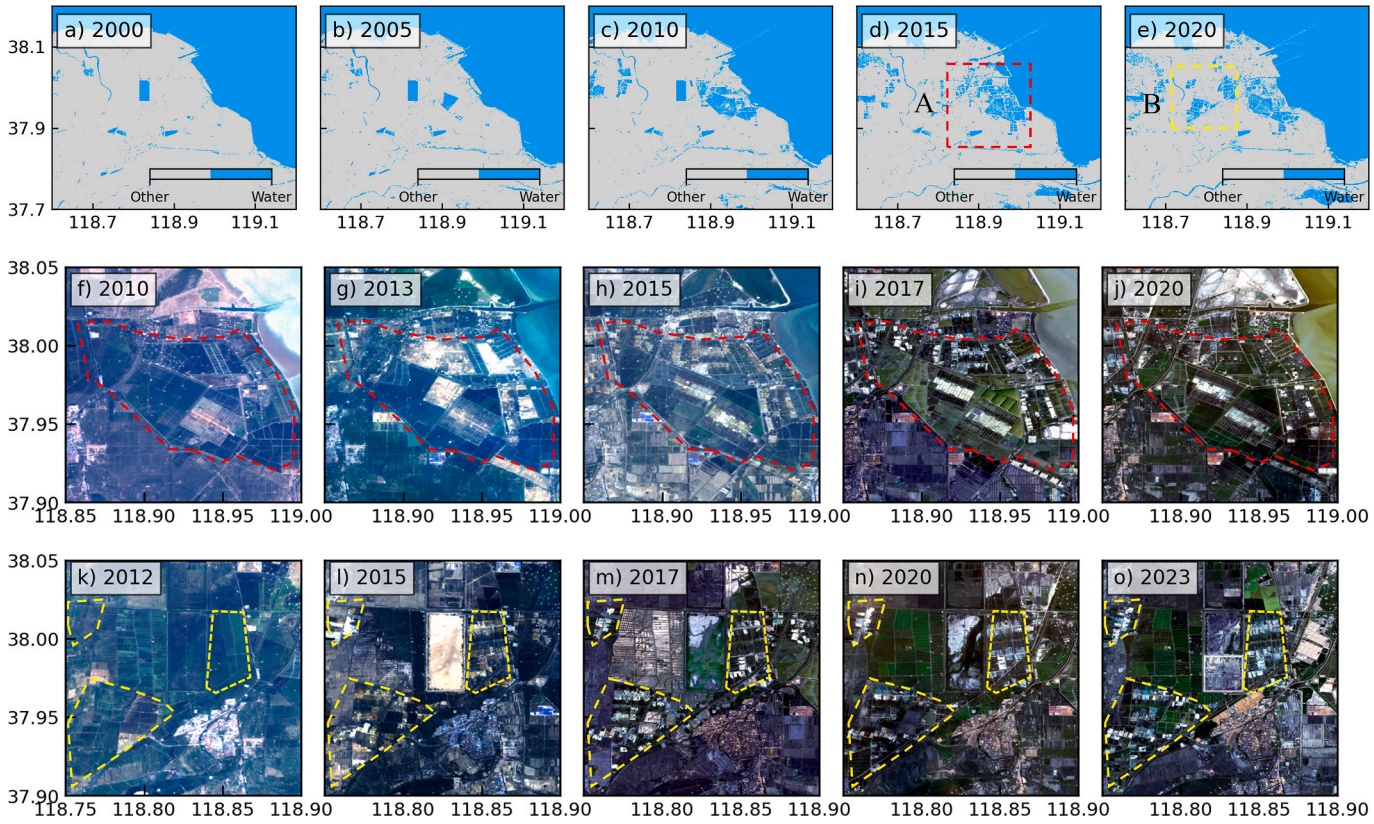

Fig. 19. Changes of land use and corresponding optical imagery in the coastal region of YRD. The dashed red and dashed yellow boxes denote the extents of satellite images in the second and third rows, respectively. Second row: the development in salt pans of Area A. Third row: development of salt pans in Area B. The dashed red and dashed yellow boxes denote the extents of satellite images in the second and third rows, respectively. The land use data are derived from Zhang et al., 2024. (For interpretation of the references to colour in this figure legend, the reader is referred to the web version of this article.)

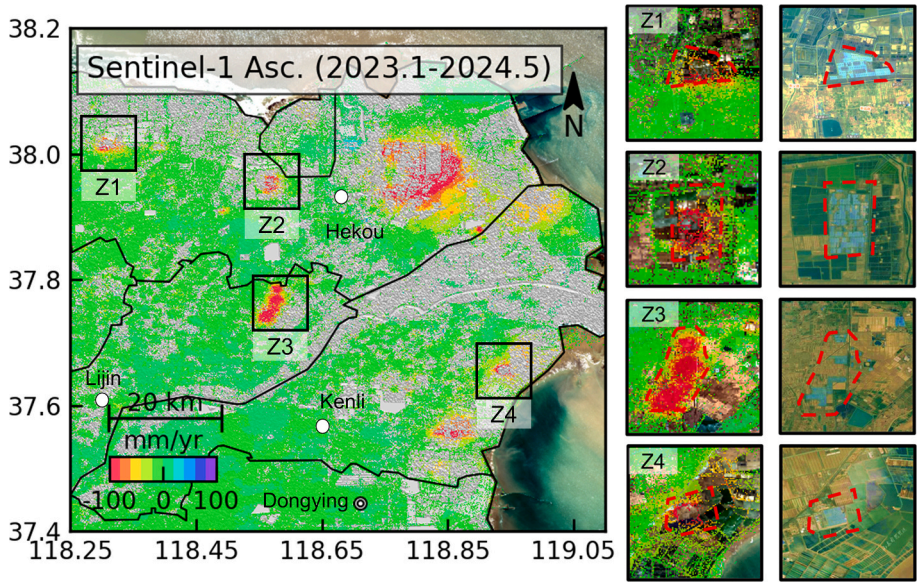

Fig. 20. The deformation rate of newly emerged small subsidence funnels Z1-Z4 since 2023.

method (Fu et al., 2025). The proposed method achieves comparable accuracy to the PEFWA method in Case II, while improving the linking accuracy by 9 % and 195 % in Case III and IV, respectively (See Table 4). Notably, exponential deformation time series linkages demonstrated the most significant accuracy enhancement. This instability arises from piecewise segment fitting without time series constraints between gaps, particularly under high-noise conditions (Fig. 22). In addition, computational efficiency of the proposed method is further evident in large-scale applications. In the YRD case with 426,841 measurement points requiring temporal linkage, the PEFWA method required 38,860 s versus 1569 s for the proposed framework, achieving a 25× speedup.

However, the proposed method is applicable when neither of the two

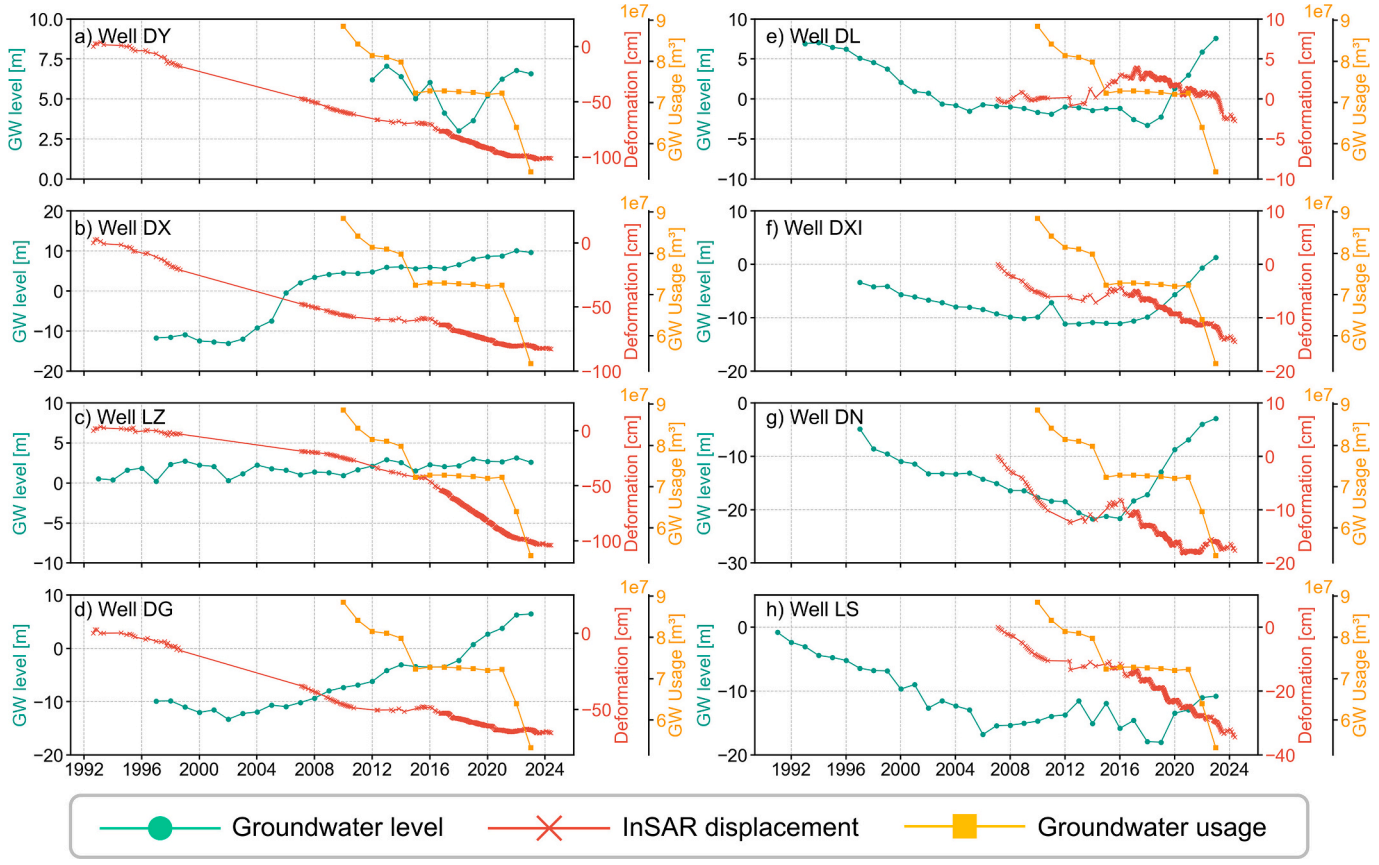

Fig. 21. Comparison between groundwater and InSAR at well sites (i.e., locations of wells can be found in Fig. 1).

Table 3
Average fitting errors and time costs for temporal linkage in Case II–IV using linear and nonlinear models.

	Number of simulated time series	Average fitting errors of linear fitting	Average fitting errors of non-linear fitting	Time of linear fitting for each entry (s)	Time of nonlinear fitting for each entry (s)
Case2 (Parabola)	2000	15.03 mm	**10.24 mm**	3.0e-5	**1.8e-5**
Case3 (Linear)	4567	**26.1 %**	38.6 %	**2.5e-5**	0.05
Case4 (Exponential)	5116	74.9 %	**38.7 %**	2.4e-5	**0.026**

*Test on Intel ® Xeon(R) W-2255 CPU with 125.5GB Ram.
**The bold texts are the results from the proposed method.

Table 4
Comparison between the proposed TAFMC method and the PEFWA method in Cases II-IV.

	Case II mean error	Case III mean error	Case IV mean error	Case II time (s)	Case III time (s)	Case IV time (s)
TAFMC	10.24 mm	26.1 %	38.7 %	1.8e-5	2.5e-5	0.026
PEFWA	10.21 mm	35.0 %	234.0 %	0.33	0.165	0.151

*Test on Intel ® Xeon(R) W-2255 CPU with 125.5GB Ram.

time series to be connected exhibits significant changes in its own deformation pattern. For cases in which either or both of the time series to be connected exhibit substantial changes in their respective deformation patterns, to ensure this condition is met in classification, we recommend selecting segments adjacent to the temporal gap rather than using the entire series. In the future, pre-classification processing steps, such as time series inflection point detection, can be integrated, to adaptively determine the length of time series segments.

5.5. *Lessons learned from three decades of InSAR monitoring in the YRD*

Long-term InSAR deformation monitoring provides a precise and detailed characterization of surface deformation in the Yellow River Delta, capturing the full cycle of anthropogenic activities and enabling more robust interpretations of deformation mechanisms. By constructing continuous deformation time series, the deformation data can be jointly analyzed with groundwater levels, oil extraction and water injection records, and brine exploitation data, thereby providing strong evidence for the identification of subsidence-driving mechanisms.

The lessons from continuous InSAR monitoring in the YRD extends beyond documenting surface subsidence and analyzing deformation mechanisms, providing valuable guidance for disaster prevention and policy-making. Deep groundwater extraction remains the primary driver of regional subsidence centers. To prevent irreversible aquifer loss and infrastructure damage, stricter regulation of groundwater extraction and timely implementation of artificial recharge in Guangrao County are recommended. Oil extraction and associated water injection have induced not only considerable vertical subsidence but also horizontal deformation, posing additional shear stresses that reduce infrastructure

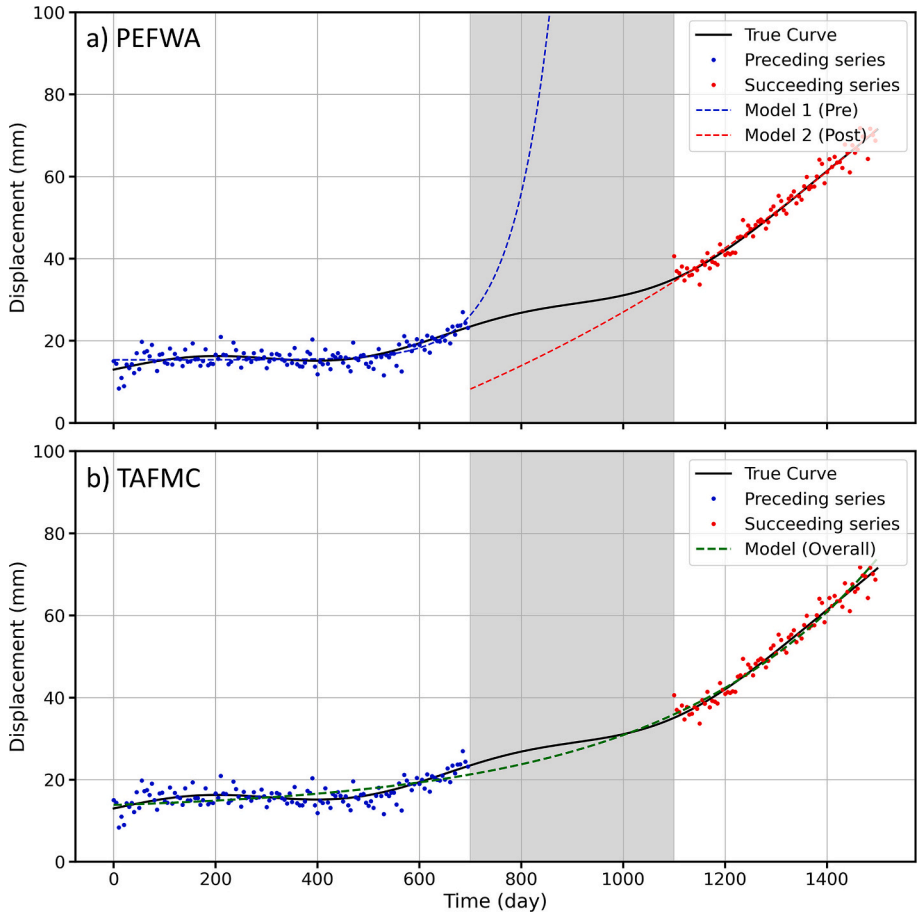

Fig. 22. Example of comparison between the PEFWA and the proposed TAFMC method.

stability. In addition, emerging forms of aquaculture, such as shrimp farming, have produced localized but severe subsidence, highlighting the urgent need for enhanced regulatory oversight.

Therefore, establishing a multi-decadal InSAR monitoring framework is essential not only for accurately quantifying deformation but also for identifying regulatory measures to control and mitigate geohazards. Fortunately, in most delta regions, even with open-archived SAR missions such as ERS-1/2 (1992–2011), Envisat (2002−2011), and Sentinel-1 (2014–present), it is feasible to conduct similar long-term InSAR analyses spanning the past 20–30 years.

6. Conclusion

This study utilized multi-source SAR data to investigate the fine-scale deformation evolution in the YRD over the past three decades. A new InSAR time series connection method, TAFMC, was proposed to provide a universal framework to link the InSAR time series with stable, linear, parabolic, and exponential trends. It also suits the large-scale application with low computational cost. Through three decades of connected InSAR time series, we identified the comprehensive deformation evolution in YRD:

1) In recent three decades (1992–2024), the cumulative subsidence of groundwater extraction zones in Guangrao County has reached 220 cm and coastal brine extraction areas in eastern Hekou County has exceeded 170 cm.
2) The coastal subsidence funnel in eastern Hekou District has shifted inland since 2021 due to the change of brine extraction, while the subsidence funnel in Guangrao County has gradually diminished due to the decreased usage of groundwater.
3) A newly small-scale funnels (11–23 km^2) have emerged in Hekou, Lijin, and Kenli districts around 2023. The new mode of aquaculture industry for shrimp, which consumes shallow brine water may be charge of the subsidence.
4) The anthropogenic activity in the YRD such as oil production, and groundwater extraction from medium and deep layers, control localized deformation patterns. These works show the capability of decadal InSAR observation and linked time series deformation in revealing the delta deformation evolution and support for the sustainable development. In future, we suggest to integrate InSAR, in-situ measurements (such as deep groundwater well and the reservoir operation log), and numerical models to further examine the deformation mechanism in YRD.

CRediT authorship contribution statement

Wenbin Xu: Writing – review & editing, Writing – original draft, Methodology, Funding acquisition, Formal analysis, Conceptualization. **Jinheng Liu:** Writing – review & editing, Writing – original draft, Visualization, Software, Methodology, Investigation, Formal analysis. **Lei Xie:** Writing – review & editing, Writing – original draft, Methodology, Investigation, Formal analysis, Conceptualization. **Mimi Peng:** Writing – review & editing, Investigation, Formal analysis. **Hao Wang:** Writing – review & editing, Formal analysis, Data curation.

Declaration of competing interest

The authors declare that they have no known competing financial interests or personal relationships that could have appeared to influence the work reported in this paper.

Acknowledgement

This research was funded by National Natural Science Foundation of China (42304037, 42174023), National Key Research and Development Program (2022YFB3903602), Natural Science Foundation of Hunan Province (2024JJ3031, 2025JJ60239), Hunan Provincial Transportation Science and Technology Progress and Innovation Plan Project (202211), the Frontier Cross Research Project of Central South University (2023QYJC006). ERS-1/2 and Envisat-ASAR data were provided by the Europe Space Agency (ESA); JERS, ALOS-1 data were provided by Japan Aerospace Exploration Agency (No. ER4A2N080 and ER4A2N102). The Copernicus Sentinel-1 data were provided by ESA and downloaded from ASF Data Vertex (https://search.asf.alaska.edu/#/).

Appendix A. Supplementary data

Supplementary data to this article can be found online at https://doi.org/10.1016/j.rse.2025.115053.

Data availability

Data will be made available on request.

References

Anthony, E., Syvitski, J., Zăinescu, F., Nicholls, R.J., Cohen, K.M., Marriner, N., Saito, Y., Day, J., Minderhoud, P.S.J., Amorosi, A., Chen, Z., Morhange, C., Tamura, T., Vespremeanu-Stroe, A., Besset, M., Sabatier, F., Kaniewski, D., Maselli, V., 2024. Delta sustainability from the Holocene to the Anthropocene and envisioning the future. Nat. Sustain. 7 (10), 1235–1246. https://doi.org/10.1038/s41893-024-01426-3.

Berardino, P., Fornaro, G., Lanari, R., Sansosti, E., 2002. A new algorithm for surface deformation monitoring based on small baseline differential SAR interferograms. IEEE Trans. Geosci. Remote Sens. 40 (11), 2375–2383. https://doi.org/10.1109/TGRS.2002.803792.

Chen, B., Gong, H., Chen, Y., Lei, K., Zhou, C., Si, Y., Li, X., Pan, Y., Gao, M., 2021. Investigating land subsidence and its causes along Beijing high-speed railway using multi-platform InSAR and a maximum entropy model. Int. J. Appl. Earth Obs. Geoinf. 96, 102284. https://doi.org/10.1016/j.jag.2020.102284.

Chen, Y., 2022. Analysis of the dynamic characteristics of groundwater levels in the over-extraction area of shallow groundwater in Guangrao County. In: 2022 China Water Resources Academic Conference (China Society of Hydrology and Water Resources 2022 Annual Conference), Beijing, China.

Cun, S., Xia, C., Yang, X., Tu, B., Li, X., 2024. Asynchronous injection-production energy supplement method to improve the oil production in the same-layer oil-water reservoir. Pet. Drill. Prod. Technol. 46 (3), 298–308. https://doi.org/10.13639/j.odpt.202407013.

Dong, J., Guo, S., Wang, N., Zhang, L., Ge, D., Liao, M., Gong, J., 2023. Tri-decadal evolution of land subsidence in the Beijing plain revealed by multi-epoch satellite InSAR observations. Remote Sens. Environ. 286, 113446. https://doi.org/10.1016/j.rse.2022.113446.

Dong, S., Samsonov, S., Yin, H., Ye, S., Cao, Y., 2014. Time-series analysis of subsidence associated with rapid urbanization in Shanghai, China measured with SBAS InSAR method. Environ. Earth Sci. 72 (3), 677–691. https://doi.org/10.1007/s12665-013-2990-y.

Duan, G., Gong, H., Chen, B., Li, X., Pan, X., Shi, M., Zhang, H., 2022. Spatiotemporal heterogeneity of land subsidence in Beijing. Sci. Rep. 12 (1), 15120. https://doi.org/10.1038/s41598-022-16674-6.

Edmonds, D.A., Toby, S.C., Siverd, C.G., Twilley, R., Bentley, S.J., Hagen, S., Xu, K., 2023. Land loss due to human-altered sediment budget in the Mississippi River Delta. Nat. Sustain. 6 (6), 644–651. https://doi.org/10.1038/s41893-023-01081-0.

Esene, C., Rezaei, N., Aborig, A., Zendehboudi, S., 2019. Comprehensive review of carbonated water injection for enhanced oil recovery. Fuel 237, 1086–1107. https://doi.org/10.1016/j.fuel.2018.08.106.

Fang, J., Nicholls, R.J., Brown, S., Lincke, D., Hinkel, J., Vafeidis, A.T., Du, S., Zhao, Q., Liu, M., Shi, P., 2022. Benefits of subsidence control for coastal flooding in China. Nat. Commun. 13 (1), 6946. https://doi.org/10.1038/s41467-022-34525-w.

Festa, D., Novellino, A., Hussain, E., Bateson, L., Casagli, N., Confuorto, P., Del Soldato, M., Raspini, F., 2023. Unsupervised detection of InSAR time series patterns based on PCA and K-means clustering. Int. J. Appl. Earth Obs. Geoinf. 118, 103276. https://doi.org/10.1016/j.jag.2023.103276.

Fialko, Y., Simons, M., Agnew, D., 2001. The complete (3-D) surface displacement field in the epicentral area of the 1999 MW7.1 Hector mine earthquake, California, from space geodetic observations. Geophys. Res. Lett. 28 (16), 3063–3066. https://doi.org/10.1029/2001GL013174.

Fu, Y., Wang, J., Zhang, Y., Yang, H., Li, L., Ren, Z., 2025. Spatiotemporal evolution characteristics of ground deformation in the Beijing plain from 1992 to 2023 derived from a novel multi-sensor InSAR fusion method. Remote Sens. Environ. 319, 114635. https://doi.org/10.1016/j.rse.2025.114635.

Haghshenas Haghighi, M., Motagh, M., 2019. Ground surface response to continuous compaction of aquifer system in Tehran, Iran: results from a long-term multi-sensor InSAR analysis. Remote Sens. Environ. 221, 534–550. https://doi.org/10.1016/j.rse.2018.11.003.

Herring, T., King, R., McClusky, S., 2010. Introduction to Gamit/Globk, 400. Massachusetts Institute of Technology, Cambridge, Massachusetts, p. 401.

Higgins, S., Overeem, I., Tanaka, A., Syvitski, J.P.M., 2013. Land subsidence at aquaculture facilities in the Yellow River delta, China. Geophys. Res. Lett. 40 (15), 3898–3902. https://doi.org/10.1002/grl.50758.

Hu, B., Li, H., Zhang, X., Fang, L., 2020. Oil and gas mining deformation monitoring and assessments of disaster: using interferometric synthetic aperture radar technology. IEEE Geosci. Remote Sens. Mag. 8 (2), 108–134. https://doi.org/10.1109/MGRS.2020.2989239.

Li, G., Zhao, C., Wang, B., Peng, M., Bai, L., 2023. Evolution of spatiotemporal ground deformation over 30 years in Xi'an, China, with multi-sensor SAR interferometry. J. Hydrol. 616, 128764. https://doi.org/10.1016/j.jhydrol.2022.128764.

Liang, Y., 2011. Study on the Improvement of Development Effects in the High-Water Cut Stage of Dongxin Fault-Block Oil Reservoir [Master's Thesis].

Liu, Y., Huang, H., 2013. Characterization and mechanism of regional land subsidence in the Yellow River Delta, China. Nat. Hazards 68 (2), 687–709. https://doi.org/10.1007/s11069-013-0648-4.

Liu, Y., Huang, H., Liu, Y., Bi, H., 2016. Linking land subsidence over the Yellow River delta, China, to hydrocarbon exploitation using multi-temporal InSAR. Nat. Hazards 84 (1), 271–291. https://doi.org/10.1007/s11069-016-2427-5.

Liu, Y., Zhang, Y., Zhao, F., Ding, R., Zhao, L., Niu, Y., Qu, F., Ling, Z., 2023. Multi-source SAR-based surface deformation monitoring and groundwater relationship analysis in the Yellow River Delta, China. Remote Sens 15 (13), 3290. https://doi.org/10.3390/rs15133290.

Lu, C., Xu, H., Yao, Q., Liu, Q., Bricker, J.D., Jonkman, S.N., Yin, J., Wang, J., 2025. Tracking 30-year evolution of subsidence in Shanghai utilizing multi-sensor InSAR and random forest modelling. Int. J. Appl. Earth Obs. Geoinf. 140, 104606. https://doi.org/10.1016/j.jag.2025.104606.

Minderhoud, P.S.J., Coumou, L., Erban, L.E., Middelkoop, H., Stouthamer, E., Addink, E. A., 2018. The relation between land use and subsidence in the Vietnamese Mekong delta. Sci. Total Environ. 634, 715–726. https://doi.org/10.1016/j.scitotenv.2018.03.372.

Park, S.-W., Hong, S.-H., 2021. Nonlinear modeling of subsidence from a decade of InSAR time series. Geophys. Res. Lett. 48 (3), e2020GL090970. https://doi.org/10.1029/2020GL090970.

Peng, M., Zhao, C., Zhang, Q., Lu, Z., Bai, L., Bai, W., 2020. Multi-scale and multi-dimensional time series InSAR characterizing of surface deformation over Shandong peninsula, China. Appl. Sci. 10 (7), 2294. https://doi.org/10.3390/app10072294.

Qu, F., Lu, Z., Kim, J., Turco, M.J., 2023. Mapping and characterizing land deformation during 2007–2011 over the Gulf coast by L-band InSAR. Remote Sens. Environ. 284, 113342. https://doi.org/10.1016/j.rse.2022.113342.

Shirzaei, M., Bürgmann, R., 2018. Global climate change and local land subsidence exacerbate inundation risk to the San Francisco Bay Area. Sci. Adv. 4 (3), eaap9234. https://doi.org/10.1126/sciadv.aap9234.

Shirzaei, M., Ojha, C., Werth, S., Carlson, G., Vivoni, E.R., 2019. Comment on "short-lived pause in Central California subsidence after heavy winter precipitation of 2017" by K. D. Murray and R. B. Lohman. Sci. Adv. 5 (6), eaav8038. https://doi.org/10.1126/sciadv.aav8038.

Syvitski, J.P.M., Kettner, A.J., Overeem, I., Hutton, E.W.H., Hannon, M.T., Brakenridge, G.R., Day, J., Vörösmarty, C., Saito, Y., Giosan, L., Nicholls, R.J., 2009. Sinking deltas due to human activities. Nat. Geosci. 2 (10), 681–686. https://doi.org/10.1038/ngeo629.

Tang, W., Zhao, X., Motagh, M., Bi, G., Li, J., Chen, M., Chen, H., Liao, M., 2022. Land subsidence and rebound in the Taiyuan basin, northern China, in the context of inter-basin water transfer and groundwater management. Remote Sens. Environ. 269, 112792. https://doi.org/10.1016/j.rse.2021.112792.

Tang, W., Gong, Z., Sun, X., Liu, Y.A., Motagh, M., Li, Z., Li, J., Malinowska, A., Jiang, J., Wei, L., Zhang, X., Wei, X., Li, H., Geng, X., 2024. Three-dimensional surface deformation from multi-track InSAR and oil reservoir characterization: a case study in the Liaohe oilfield, Northeast China. Int. J. Rock Mech. Min. Sci. 174, 105637. https://doi.org/10.1016/j.ijrmms.2024.105637.

Wang, G., Li, P., Li, Z., Liang, C., Wang, H., 2022a. Coastal subsidence detection and characterization caused by brine mining over the Yellow River Delta using time series InSAR and PCA. Int. J. Appl. Earth Obs. Geoinf. 114, 103077. https://doi.org/10.1016/j.jag.2022.103077.

Wang, Y., Feng, G., Li, Z., Xu, W., Zhu, J., He, L., Xiong, Z., Qiao, X., 2022b. Retrieving the displacements of the Hutubi (China) underground gas storage during 2003–2020 from multi-track InSAR. Remote Sens. Environ. 268, 112768. https://doi.org/10.1016/j.rse.2021.112768.

Werner, C., Wegmüller, U., Strozzi, T., Wiesmann, A., 2000. Gamma SAR and Interferometric Processing Software. Proceedings of the Ers-Envisat Symposium, Gothenburg, Sweden.

Xing, X., Zhang, T., Zhu, J., Shi, J., Cai, J., Zheng, G., Lei, M., 2024. Quantitative prediction for deformation and brine extraction in salt solution mining based on water-solution kinetic (WSK) InSAR model. IEEE J. Sel. Top. Appl. Earth Obs. Remote Sens 17, 7655–7673. https://doi.org/10.1109/JSTARS.2023.3348210.

Yu, C., Li, Z., Penna, N.T., Crippa, P., 2018. Generic atmospheric correction model for interferometric synthetic aperture radar observations. J. Geophys. Res. Solid Earth 123 (10), 9202–9222. https://doi.org/10.1029/2017JB015305.

Zhang, B., Wang, R., Deng, Y., Ma, P., Lin, H., Wang, J., 2019a. Mapping the Yellow River Delta land subsidence with multitemporal SAR interferometry by exploiting both persistent and distributed scatterers. ISPRS J. Photogramm. Remote Sens. 148, 157–173. https://doi.org/10.1016/j.isprsjprs.2018.12.008.

Zhang, J., Huang, H., Bi, H., 2015. Land subsidence in the modern Yellow River Delta based on InSAR time series analysis. Nat. Hazards 75 (3), 2385–2397. https://doi.org/10.1007/s11069-014-1434-7.

Zhang, X., Zhao, T., Xu, H., Liu, W., Wang, J., Chen, X., Liu, L., 2024. GLC_FCS30D: the first global 30 m land-cover dynamics monitoring product with a fine classification system for the period from 1985 to 2022 generated using dense-time-series Landsat imagery and the continuous change-detection method. Earth Syst. Sci. Data 16 (3), 1353–1381. https://doi.org/10.5194/essd-16-1353-2024.

Zhang, Y., Liu, Y., Zhang, X., Huang, H., Qin, K., Bai, Z., Zhou, X., 2021. Correlation analysis between land-use/cover change and coastal subsidence in the Yellow River Delta, China: reviewing the past and prospecting the future. Remote Sens 13 (22), 4563. https://www.mdpi.com/2072-4292/13/22/4563.

Zhang, Y., Luo, Y., Huang, H., Liu, Y., Bi, H., Zhang, X., Zhang, Z., Wang, K., Bai, Z., Zhou, X., 2023. Correlating severe land subsidence and confined brine aquifer compaction in the Yellow River Delta, China, with sentinel-1A/1B satellite images. Mar. Georesour. Geotechnol. 41 (8), 927–934. https://doi.org/10.1080/1064119X.2022.2109537.

Zhang, Y., Si, Z., Lin, X., Zhang, Z., Chu, H., Cao, C., Liu, Y., Huang, H., Huang, B., Bai, Z., Wang, K., Zhou, X., Song, Z., 2024b. Time-series InSAR reveals new insights into land subsidence in the Yellow River Delta, China. Mar. Georesour. Geotechnol. 1–10. https://doi.org/10.1080/1064119X.2024.2335678.

Zhao, D., Chen, B., Gong, H., Lei, K., Zhou, C., Hu, J., 2024. Unraveling the deformation and water storage characteristics of different aquifer groups by integrating PS-InSAR technology and a spatial correlation model. IEEE J. Sel. Top. Appl. Earth Obs. Remote Sens. 17, 2501–2515. https://doi.org/10.1109/JSTARS.2023.3323699.